UNIVERSIDAD DE CONCEPCIÓN
FACULTAD DE CIENCIAS FÍSICAS Y MATEMÁTICAS

From Formation to Quenching: The Role of Overdensities in High-Redshift Galaxy Evolution

By: Matias Espinoza

Thesis presented to the Faculty of Physical and Mathematical Sciences of the University of Concepción for the academic degree of Master in Astronomy.

March 2024
Concepción, Chile

Tutor: Ricardo Demarco and Lucia Guaita

Acknowledgment

ME and LG would like to express their gratitude for the financial support provided by the FONDECYT regular project, number 1230591. We extend our heartfelt thanks to Alain Andrade, Ian Baeza, Benjamin Jara Bravo, and Sarath Satheesh Sheeba for their invaluable discussions and insights.

Additionally, R.D. would like to sincerely acknowledge the support received from the ANID BASAL project FB210003, which has significantly contributed to this research.

Resume

This study investigates the evolution of galaxies within 13 overdensities at redshifts $3 < z < 4$, providing critical insights into galaxy formation and evolution in dense environments. Key findings include the observation that passive galaxies in these protoclusters are rare, with only two overdensities containing them. These passive galaxies are distinguished by their redder color, greater mass, older age, lower star formation rates, and higher stellar density. A notable discovery is the exclusive presence of AGNs in overdensities with passive galaxies, hinting at a potential correlation between AGN activity and the presence of passive galaxies. Spatial analysis underlines that passive galaxies predominantly occupy the highest density peaks within these overdensities. Comparisons with TNG300 simulations suggest that protoclusters with early passive galaxies are likely to evolve with a higher fraction of passive galaxies at lower redshifts. The estimated Dark Matter Halo values for these overdensities correspond with protocluster expectations. This research significantly advances our understanding of the role of dense environments in galaxy evolution, particularly highlighting the development of passive galaxies within protoclusters and offering new perspectives on environmental impacts on galactic evolution and early universe structure formation.

Keywords –

Abstract

Exploring galaxy evolution in dense environments, particularly within protoclusters, is pivotal for understanding the mechanisms driving star formation and quenching. This research provides insights into how the environment, especially in dense protoclusters, significantly impacts galaxy evolution, affecting properties such as star formation rates, mass build-up, and galaxy morphology. This study focuses on characterizing galaxies in the overdensities identified in the Chandra Deep Field South (CDFS) and Ultra Deep Survey (UDS) regions, at 3<z<4, with the aim of investigating the influence of environment on galaxy evolution. Our methodology involves a detailed spectral energy distribution (SED) analysis of galaxies, using data from the VANDELS survey. We employed Bayesian analysis techniques, specifically BEAGLE and BAGPIPES tools, to obtain the best-fit parameters for the SED of each galaxy. This approach allowed us to accurately determine star formation rates, masses, and ages of the galaxies, complemented by the UVJ diagram and sSFR (Specific Star Formation Rate) criterion for classification. We found that galaxies in overdensities at 3<z<4 exhibit distinct properties compared to those in less dense field galaxies. Specifically, passive galaxies in overdensities are redder, more massive, show lower sSFR, lower star formation surface densities, and a compact morphology. The overdensities hosting these passive galaxies at z=3 have dark matter halo masses consistent with being protoclusters and contain AGN. The environment around passive galaxies in overdensities is denser than around passive galaxies in the field, aligning with them being located in the highest density peaks. Using the TNG300 simulation, we find that protocluster structures with a passive galaxy at high redshift are more likely to evolve with a higher fraction of passive galaxies by $z = 0.6$. By following the evolution of a passive galaxy in a protocluster at $z = 3$, we observed that its sSFR was significantly high up to $z = 6$, after which it began to decline. Also, the stellar mass of this passive galaxy was rapidly assembled from z = 6 to z = 3. These characteristics are consistent with the ones of the passive galaxies we observed in our $z \sim 3$ overdensities.

Keywords –

Contents

Acknowledgment i

Resume ii

Abstract iii

1 Introduction 1

2 Theoretical Framework 4
2.1 Galaxy and Protocluster Formation Theories 4
2.2 Role of Dark Matter Halo Mass and Volume in Galaxy Evolution . . . 4
2.3 Protocluster Identification and Analysis Methods 5
2.4 Importance of Passive Galaxies in Protoclusters 5
2.5 Comparative Analysis with Previous Studies and Simulations 5
2.6 Key References and Relevant Theories 5

3 Methodology 7
3.1 Spectral Energy Distribution Analysis with BEAGLE 7
3.2 Redshift Estimation and Protocluster Identification 8
3.2.1 Gemini GMOS Data Acquisition and Reduction 8
3.3 AGN Identification and Morphological Analysis 10
3.4 Methodology 12
3.5 Filter Convolutions and UVJ Diagram Reconstruction 12
3.6 Selection Criteria for Passive Galaxies 12
3.7 Passive galaxies from literature 14

4 Analysis 15
4.1 Properties of the overdensities at $3 < z < 4$ 15
4.2 Scaling Relations 17

5 Discussion 24
5.1 Overdensity $z355$ 26
5.2 Overdensity $z343$ 28
5.3 Comparison with Previous Studies 28
5.4 Comparison with TNG300 29

5.4.1 Accessing TNG300 Simulation Data 30
5.4.2 Learning to Work with TNG Data 30
5.4.3 Selection of Protoclusters 30
5.4.4 Programming for Data Extraction 30
5.4.5 Analysis of Passive Galaxies Across Redshifts 30

6 Conclusion **32**

Bibliography **35**

Appendix **42**

A Other Plots **42**
A1 UVJ Diagram 42
A2 Redshift Distribution 44

List of Tables

4.1.1 Presents detailed information on the identified protoclusters, including central coordinates, names, volumes, and halo masses. 15

List of Figures

3.2.1 Histogram of redshift distributions for the $z355$ overdensity. The distribution of photometric redshifts is illustrated in royal blue, while the distribution of spectroscopic redshifts is depicted in dark magenta. This histogram provides a comparative view of the redshift variations within the overdensity, highlighting the alignment and discrepancies between photometric and spectroscopic measurements. 9

3.2.2 Two-dimensional GMOS spectrum showcasing an observed continuum not aligned with the intended target, indicating a low-redshift source. The spectrum displays a distinct feature where the continuum is not centered, suggesting the presence of an unexpected astronomical object in the field of view. The horizontal axis represents the wavelength in Å, while the vertical axis corresponds to the spatial dimension in pixels. This unanticipated observation highlights the complexity and challenges of astronomical spectroscopy, particularly in crowded fields or when dealing with faint targets. 11

3.5.1 Comparison of Spectral Energy Distributions (SEDs) computed by BEAGLE for two galaxy types. The upper panel displays the SED of a passive galaxy (green line). In contrast, the lower panel shows the SED of a star-forming galaxy (navy line). The U, V, and J filters, utilized for calculating photometric magnitudes, are marked on each graph to highlight the spectral regions where these galaxies exhibit significant differences in the rest-frame. 13

4.1.1 Multiple UVJ diagrams showcasing galaxies in various conditions. Upper left: member galaxies from protoclusters excluding those with passive galaxies. Upper center: protocluster at z=3.55. Upper right: protocluster at z=3.43. Lower left: field galaxies associated with protocluster z=3.55. Lower right: field galaxies associated with protocluster z=3.43. The color scale denotes log(sSFR), with red signifying lower values and blue higher ones. Different shapes represent the nature of the galaxies: triangles for spectroscopic redshift, dots for photometric redshift, diamonds for AGN, and green crosses for passive galaxies. The lines in the diagrams outline the classification criteria set by Williams et al. (2009) and Whitaker et al. (2011). 16

4.2.1 Star Formation Rate (SFR) plotted against stellar mass for various galaxy samples. Upper left: member galaxies from protoclusters excluding those with passive galaxies. Upper center: protocluster at z=3.55. Upper right: protocluster at z=3.43. Lower left: field galaxies associated with protocluster z=3.55. Lower right: field galaxies associated with protocluster z=3.43. Different symbols represent the nature of the galaxies: triangles for galaxies with spectroscopic redshift, dots for those with photometric redshift, diamonds for AGN, and crosses for passive galaxies. 18
4.2.2 (U-V) rest frame vs Mass diagrams of galaxies under various conditions. Upper left: member galaxies from protoclusters excluding those with passive galaxies. Upper center: protocluster at z=3.55. Upper right: protocluster at z=3.43. Lower left: field galaxies associated with protocluster z=3.55. Lower right: field galaxies associated with protocluster z=3.43. Different shapes represent the nature of the galaxies: triangles for spectroscopic redshift, dots for photometric redshift, diamonds for AGN, and crosses for passive galaxies. 19
4.2.3 Surface density SFR vs Mass diagrams of galaxies under various conditions. Upper left: member galaxies from protoclusters excluding those with passive galaxies. Upper center: protocluster at z=3.55. Upper right: protocluster at z=3.43. Lower left: field galaxies associated with protocluster z=3.55. Lower right: field galaxies associated with protocluster z=3.43. Different shapes represent the nature of the galaxies: triangles for spectroscopic redshift, dots for photometric redshift, diamonds for AGN, and crosses for passive galaxies. 20
4.2.4 Tau/Age vs Age diagrams of galaxies under various conditions. Upper left: member galaxies from protoclusters excluding those with passive galaxies. Upper center: protocluster at z=3.55. Upper right: protocluster at z=3.43. Lower left: field galaxies associated with protocluster z=3.55. Lower right: field galaxies associated with protocluster z=3.43. Different shapes represent the nature of the galaxies: triangles for spectroscopic redshift, dots for photometric redshift, diamonds for AGN, and crosses for passive galaxies. 21
4.2.5 Size vs Mass diagrams of galaxies under various conditions. Upper left: member galaxies from protoclusters excluding those with passive galaxies. Upper center: protocluster at z=3.55. Upper right: protocluster at z=3.43. Lower left: field galaxies associated with protocluster z=3.55. Lower right: field galaxies associated with protocluster z=3.43. Different shapes represent the nature of the galaxies: triangles for spectroscopic redshift, dots for photometric redshift, diamonds for AGN, and crosses for passive galaxies. The lines on the diagram are based on the criteria set by van der Wel et al. (2014) 23

5.0.1 Spatial Distribution of Galaxy Counts in Overdensities. **Left:** Distribution relative to the passive galaxy ($z343$ in cyan, $z355$ in black, $z323$ in orange). **Right:** Distribution showing distinct groups within the overdensities (Groups A, B, C differentiated by dashed lines). These visualizations collectively depict the spatial dynamics and group formations around passive galaxies in various cosmic environments. . 25
5.1.1 Spatial Distribution and Kernel Density Estimations of the z355 Overdensity. The central plot displays the RA and DEC scatter plot, illustrating the spatial distribution of galaxies within the z355 overdensity. The galaxies are represented with different symbols based on their redshift types: circles for photometric redshift and downward triangles for spectroscopic redshift. Additionally, AGNs are denoted by diamonds. On the margins, kernel density estimations are presented: to the right for DEC, and at the top for RA. These density estimations provide an intuitive view of the concentration and dispersion of galaxies along each axis, highlighting the distinct spatial characteristics and the AGN distribution within the z355 overdensity. 27
5.1.2 Comprehensive Spatial and Redshift Analysis of the z355 Overdensity. **Left:** The RA-DEC distribution of galaxies showcases the spatial segregation of groups A (yellow), B (red), and C (purple) within z355, using distinct symbols to represent photometric redshifts (circles), spectroscopic redshifts (downward triangles), AGNs (diamonds), and passive galaxies (crosses in green, with green stars marking those identified in previous literature). **Right:** The redshift distribution histogram for each group in the z355 overdensity, highlighting how each group's composition varies across redshifts. Vertical lines in the histogram represent the redshifts at which the passive galaxies in each group are located, with colors corresponding to their respective groups. 28
5.3.1 Age vs Mass diagram. Navy points represent members of protoclusters in CDFS. Green points denote passive galaxies. Light gray points correspond to passive galaxies from Merlin et al. (2019), while dark gray points represent passive galaxies from Straatman et al. (2014). . . 29
5.4.1 Passive Galaxy Fraction as a Function of Redshift. This graph illustrates the evolutionary trend in the fraction of passive galaxies across different redshifts. Red points denote data for cluster GrNr15, while blue points represent cluster GrNr11. The analysis underscores the influence of early passive galaxy formation in cluster GrNr11. 31

A1.1 UVJ diagram showcasing member galaxies from protoclusters in the Chandra Deep Field South (CDFS). The color scale denotes log(sSFR), where red signifies lower values, and blue represents higher ones. Different shapes indicate the nature of the galaxies: triangles for spectroscopic redshift, dots for photometric redshift, diamonds for AGN, and crosses for passive galaxies. Lines on the diagram demarcate the criteria set by Williams et al. (2009) and Whitaker et al. (2011) for classification. 42

A1.2 UVJ diagram showcasing member galaxies from protoclusters in the Ultra Deep Survey (UDS). The color scale denotes log(sSFR), where red signifies lower values, and blue represents higher ones. Different shapes indicate the nature of the galaxies: triangles for spectroscopic redshift, dots for photometric redshift. Lines on the diagram demarcate the criteria set by Williams et al. (2009) and Whitaker et al. (2011) for classification. 43
A1.3 UVJ diagram of field galaxies from protoclusters in the Chandra Deep Field South (CDFS). The color scale represents log(sSFR), with red indicating lower values and blue indicating higher values. Different shapes indicate the nature of the galaxies: triangles for spectroscopic redshift, dots for photometric redshift, diamonds for AGN, and crosses for passive galaxies. Lines on the diagram demarcate the criteria set by Williams et al. (2009) and Whitaker et al. (2011) for classification. . . 43
A2.1 Histograms of redshift distributions for all identified overdensities in the CDFS region (except $z355$). Each histogram represents a different overdensity, showcasing the variations in redshift within these structures. For each overdensity, the distribution of photometric redshifts is illustrated in royal blue, while the distribution of spectroscopic redshifts is depicted in dark magenta. 44
A2.2 Histograms of redshift distributions for all identified overdensities in the UDS region. Each histogram represents a different overdensity, showcasing the variations in redshift within these structures. For each overdensity, the distribution of photometric redshifts is illustrated in royal blue, while the distribution of spectroscopic redshifts is depicted in dark magenta. 45

Chapter 1

Introduction

The study of galaxies in dense environments, such as protoclusters, plays a crucial role in our understanding of galaxy evolution. These structures, which are the precursors to local galaxy clusters, provide a unique insight into the early stages of galaxy formation, evolution, and quenching mechanisms. Protoclusters are particularly interesting because they represent a transitional phase in the cosmic structure formation, where galaxies are undergoing significant changes in their properties (Gunn and Gott, 1972; Dressler et al., 1997; Balogh et al., 1999; Ebeling et al., 2001; Weinmann et al., 2006; Olsen et al., 2007; Wetzel et al., 2012; Menanteau et al., 2013; Wetzel et al., 2013).

Our research is focused on exploring the overdensities in the Chandra Deep Field South (CDFS) and Ultra Deep Survey (UDS) regions. These regions are known for their rich data sets, which allow for an in-depth analysis of galaxy properties and behaviors in different environments. By examining these overdensities, we aim to uncover the roles that external and internal factors play in the evolutionary processes of galaxies (Chiang et al., 2013).

One of the primary areas of interest in galaxy evolution studies is understanding the mechanisms behind star formation quenching. This phenomenon, where galaxies abruptly stop forming new stars, has been a subject of extensive research, and various mechanisms have been proposed. These include feedback from active galactic nuclei (AGN), environmental effects such as halo quenching, and internal changes within the galaxies themselves (Shahidi et al., 2020; Feldmann and Mayer, 2015; Fabian, 2012; Schawinski et al., 2007; Peng and Renzini, 2020; Johansson et al., 2009; Dekel and

Birnboim, 2008; Hopkins et al., 2012; Collins and Read, 2022; Lu et al., 2021; Kim et al., 2018). The observation of passive galaxies, which are galaxies with little to no star formation, at high redshifts challenges our traditional understanding of how galaxies evolve in dense environments (Merlin et al., 2019; Straatman et al., 2014; Shahidi et al., 2020; Schreiber et al., 2018; Carnall et al., 2018a).

Peng and Renzini (2020) underscore the significance of discerning the mechanisms driving the modulation of star formation within galaxy clusters. A pivotal shift in this research domain focuses on the investigation of quenching mechanisms in disk galaxies, particularly the role of angular momentum in hindering radial gas flows. This perspective gains support from observational data on the HI content in central disk galaxies. Insights gleaned from the ALFALFA survey and complementary studies reveal that quenched disk galaxies, within certain mass ranges, possess atomic hydrogen levels comparable to those found in actively star-forming disks. Yet, these quenched disks are characterized by a conspicuous absence of molecular H2 gas (Giovanelli et al., 2005).

This observation prompts a crucial inquiry: what intrinsically differentiates a star-forming disk from its quenched counterpart when their HI content appears analogous? Peng and Renzini (2020) introduces a novel model for disk galaxy quenching, anchored in the concept of angular momentum inhibition impeding radial flows. This model posits that the growth and subsequent quenching of disk galaxies are intrinsically linked, stemming from the accretion of co-rotating inflows that exhibit a gradual escalation in angular momentum. Such dynamics culminate in the accumulation of cold, atomic gas in orbits marked by excessively high angular momentum, thereby hindering its inward movement and precluding its contribution to ongoing star formation processes.

Our findings, which align with recent observations of passive galaxies at high redshifts, challenge the conventional models of galaxy evolution in dense environments. The presence of AGN in these areas indicates complex dynamics between supermassive black holes and their host galaxies, impacting star formation processes and potentially contributing to the quenching phenomenon.

In this thesis, we also explore the implications of angular momentum inhibition on galaxies at different stages of their evolutionary cycle. This mechanism, which leads to

quenching due to an accumulation of high angular momentum gas, appears to primarily affect more mature galaxies. This observation ties into broader paradigms of galaxy evolution and quenching, such as the mass quenching model proposed by Peng et al. (2010).

The organization of this thesis is as follows: Chapter 2 presents the theoretical framework underlying our study; Chapter 3 details our analytical methods and the data utilized; Chapter 4 discusses our findings in the context of existing theories and simulations; and Chapter 5 concludes with a summary of our results and suggestions for future research in this field.

Chapter 2

Theoretical Framework

2.1 Galaxy and Protocluster Formation Theories

Understanding the formation and evolution of galaxies within protoclusters is essential for astrophysical studies. Current theories suggest that dense environments, like those found in protoclusters, significantly influence the physical properties and evolutionary trajectories of galaxies. These models describe the complex interactions between galaxies and their environments, emphasizing factors such as dark matter density and the presence of Active Galactic Nuclei (AGNs), which play a pivotal role in galaxy formation and evolution (Overzier, 2016).

2.2 Role of Dark Matter Halo Mass and Volume in Galaxy Evolution

The mass of the dark matter halo and the volume of a protocluster are critical determinants in shaping the characteristics of galaxies. These parameters influence the gravitational potential within the protocluster, affecting the dynamics of gas and stars within galaxies. Consequently, they have a significant impact on star formation rates, morphological evolution, and overall galaxy properties (Wechsler and Tinker, 2018). Understanding these factors is crucial for comprehending the complex processes governing galaxy evolution in dense environments.

2.3 Protocluster Identification and Analysis Methods

Identifying and analyzing protoclusters requires a variety of techniques, including the analysis of redshift distributions and the estimation of dark matter halo masses. These methods are essential for characterizing the spatial distribution and mass density of protoclusters, thereby providing insights into their formation, structure, and evolution (Chiang et al., 2013). Accurate identification and analysis are fundamental for the study of galaxy evolution in these dense cosmic environments.

2.4 Importance of Passive Galaxies in Protoclusters

The study of passive galaxies in protoclusters is pivotal in understanding galaxy evolution. The presence of these galaxies in dense environments is indicative of periods of intense star formation followed by rapid quenching. Exploring the mechanisms leading to this rapid quenching in dense environments is critical for unraveling the evolutionary history of galaxies (Valentino et al., 2020).

2.5 Comparative Analysis with Previous Studies and Simulations

Comparing our findings with previous studies is crucial for contextualizing our results within the larger framework of galaxy evolution. Aligning observational data with predictions from cosmological simulations, such as those by Chiang et al. (2013) and Behroozi et al. (2013), helps validate or challenge existing models of galaxy formation and evolution in protoclusters.

2.6 Key References and Relevant Theories

Our analysis is grounded in key studies and theories in the field of astrophysics and cosmology. These include the work of van der Burg et al. (2014), which provides a

foundational understanding of dark matter halo mass estimations and their implications for galaxy formation and evolution in dense cosmic environments.

Chapter 3

Methodology

The data used in this work are from the deep VIMOS survey of the CANDELS CDFS and UDS fields (VANDELS). We took advantage of the comprehensive photometric catalog (Pentericci et al., 2018; McLure et al., 2018; Garilli et al., 2021; Talia et al., 2023), that includes photometric redshifts and a variety of physical properties, such as stellar mass, Star Formation Rates (SFR), Mass Weighted Age, Star Formation Time Scale (Tau), specific Star Formation Rate (sSFR).

Our study utilized the identified overdense structures (Guaita et al., 2020) within the VANDELS fields. We updated the redshifts of the overdensity members and field galaxies to the most recent spectroscopic redshift from VANDELS and we consider the most updated compilation made by Nimish Hathi (priv. comm.) for the VANDELS collaboration.

3.1 Spectral Energy Distribution Analysis with BEAGLE

The physical properties in the VANDELS photmetric catalog were estimated using the BEAGLE (BayEsian Analysis of GaLaxy sEds) tool (Chevallard and Charlot, 2016). The spectral energy distribution(SED) of galaxies is represented by a rich array of variety over 500 potential models.

BEAGLE incorporates both stellar and nebular emission components. Nebular emission is represented by following the Gutkin et al. (2016) approach with a Chabrier IMF. The star formation history (SFH) is represented by an exponentially delayed form, $SFR(t) \propto t \cdot exp(-t/\tau)$, where t is the age of the galaxy and τ the e-folding time of the stellar population. When $\tau = t$, the galaxy has just reached the peak of star formation; when $\tau > t$, the galaxy is observed during the star formation period; when $\tau < t$, the galaxy is observed after the peak of the main episode of star formation. The configuration of BEAGLE used in our analysis is based on the settings described in Calabrò et al. (2022) and Castellano et al. (2023).

3.2 Redshift Estimation and Protocluster Identification

Our approach to redshift estimation leverages the comprehensive data from the VANDELS collaboration catalog. A crucial step is the update of redshifts, replacing photometric to new spectroscopic ones. The extensive coverage and depth of the VANDELS survey in the CDFS and UDS fields, coupled with high levels of completeness in photometric catalogs, enable us to construct a robust and comprehensive redshift framework for our study. Fig. 3.2.1 presents the histogram of the redshift distributions for one of the overdensities, illustrating the distribution of photometric (in royal blue) and spectroscopic (in dark magenta) redshifts. The number of spectroscopic and photometric redshifts for each overdensity is detailed in Table 4.1.1. Histograms of redshift distributions for other overdensities are provided in Fig A2.1 and A2.2.

3.2.1 Gemini GMOS Data Acquisition and Reduction

For the $z355$ overdensity, we further enhanced our analysis by obtaining additional data using the Gemini Multi-Object Spectrograph (GMOS) at the Gemini Observatory. This involved a dedicated trip to La Serena, where I underwent training in data reduction techniques. The complexity of the data, coupled with the challenge presented by a damaged detector, required an intensive learning and application process using the Image Reduction and Analysis Facility (IRAF).

Despite the initial complications, we developed a strategy to address the issues

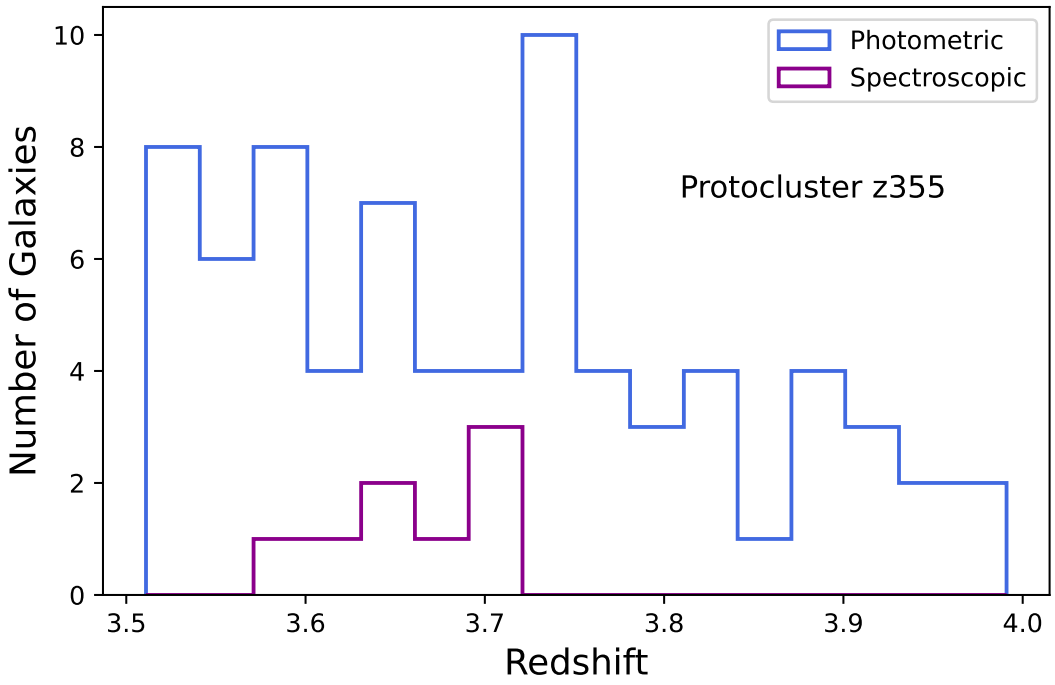

Figure 3.2.1: Histogram of redshift distributions for the $z355$ overdensity. The distribution of photometric redshifts is illustrated in royal blue, while the distribution of spectroscopic redshifts is depicted in dark magenta. This histogram provides a comparative view of the redshift variations within the overdensity, highlighting the alignment and discrepancies between photometric and spectroscopic measurements.

posed by the damaged detector. This involved the implementation of Python scripts to perform image stacking. Our goal was to mitigate the impact of the damaged detector by selectively processing the data, ensuring that it did not adversely affect the final composite image. This approach allowed us to effectively combine the reduced images while minimizing the contribution of the damaged areas, thus maintaining the integrity of our analysis.

However, despite these extensive efforts, we faced significant challenges in detecting the astronomical sources within the $z355$ overdensity. The sources were exceedingly faint, making it difficult to discern a clear continuum (Fig. 3.2.2). This underscored the inherent challenges in observing high-redshift galaxies, particularly in dense environments like protoclusters. Although the data from GMOS provided valuable insights, the weak nature of the sources limited the extent to which we could analyze their characteristics in detail. Nevertheless, the data obtained contributed to our understanding of the complexities involved in studying distant galaxy clusters and protoclusters.

3.3 AGN Identification and Morphological Analysis

We used X-ray catalogs from the literature to identify AGN, employing cross-referencing techniques with the catalogs of Kocevski et al. (2018) for UDS and Luo et al. (2017) for CDFS. Additionally, we use the VANDELS catalog of emission line AGN for further cross-referencing. Through this comparison process, we found AGN in our CDFS overdensities.

We used the catalog from van der Wel et al. (2012) to associate an half-light radius to the members of the overdensities and field galaxies. The radius was calculated using photometry in filter F160 and the algorithm GALFIT (On the HST F160W imaage).

We utilized images from the Hubble Space Telescope (HST) to confirm the sizes of galaxies as compared to those listed in the morphological catalog. Specifically, we focus on verifying our passive galaxies, namely CDFS004503 and CDFS019883.

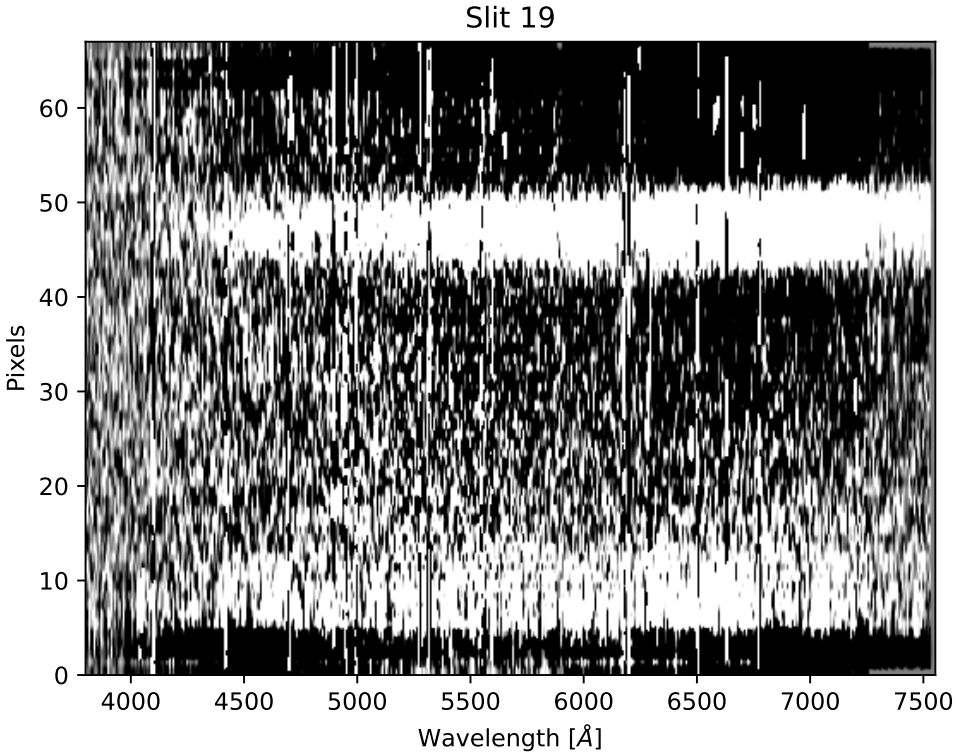

Figure 3.2.2: Two-dimensional GMOS spectrum showcasing an observed continuum not aligned with the intended target, indicating a low-redshift source. The spectrum displays a distinct feature where the continuum is not centered, suggesting the presence of an unexpected astronomical object in the field of view. The horizontal axis represents the wavelength in Å, while the vertical axis corresponds to the spatial dimension in pixels. This unanticipated observation highlights the complexity and challenges of astronomical spectroscopy, particularly in crowded fields or when dealing with faint targets.

3.4 Methodology

3.5 Filter Convolutions and UVJ Diagram Reconstruction

The construction of an accurate UVJ diagram is pivotal to our study as it allows the discrimination between star-forming and quiescent galaxies, important to understand the evolutionary state of the galaxies within our overdensities. As illustrated in Figure 3.5.1, the Spectral Energy Distributions (SEDs) computed by BEAGLE reveal distinct characteristics for these two types of galaxies. A passive galaxy exhibit a higher flux at longer wavelengths (red end of the spectrum), as opposed to the star-forming galaxy which present increased flux at shorter wavelengths (blue end). This is quantitatively reflected in their respective U-V and V-J rest-frame color values, with the passive galaxy having U-V=1.34 and V-J=0.61, while the star-forming galaxy has U-V=0.17 and V-J=-0.21. Following the approach of Williams et al. (2009), we utilized specific filters to reconstruct the UVJ diagram that captures the intrinsic properties of galaxies. The challenge was to identify the most representative SED model for each galaxy needed to obtain Mass, Star Formation Rate (SFR), Tau, Mass Weighted Age and A_V. Our methodology involved selecting an SED that best incorporated the physical properties of galaxies, guided by the median values provided by the BEAGLE software. This allowed for the reliable determination of U, V, and J rest-frame magnitudes.

3.6 Selection Criteria for Passive Galaxies

We used the UVJ diagram, as shown in Fig. A1.1 and Fig. A1.2, for identifying passive and star-forming galaxies. We relied on the criteria established by Williams et al. (2009). Additionally, we incorporated criteria based on low specific star formation rates (sSFR) as suggested by Carnall et al. (2019). Using these criteria, we identified several candidates as passive galaxies. To corroborate their low sSFR, we re-performed the SED fitting by using the BAGPIPES (Carnall et al., 2018b) software, which confirm the low sSFR of the passive galaxy candidates.

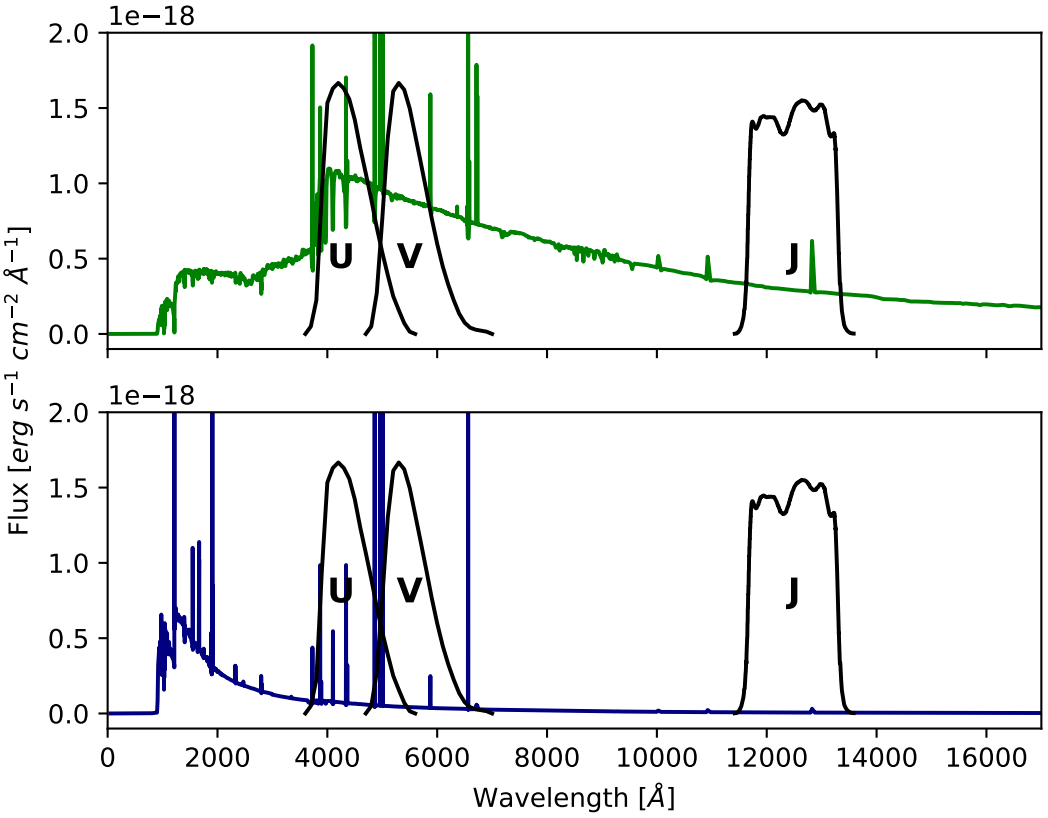

Figure 3.5.1: Comparison of Spectral Energy Distributions (SEDs) computed by BEAGLE for two galaxy types. The upper panel displays the SED of a passive galaxy (green line). In contrast, the lower panel shows the SED of a star-forming galaxy (navy line). The U, V, and J filters, utilized for calculating photometric magnitudes, are marked on each graph to highlight the spectral regions where these galaxies exhibit significant differences in the rest-frame.

3.7 Passive galaxies from literature

We conducted a crossmatch with several catalogs of passive galaxies from the literature, specifically Merlin et al., 2019, Schreiber et al., 2018, Shahidi et al., 2020, and Straatman et al., 2014. This crossmatch resulted in the identification of 10 galaxies in our sample that were previously recognized in the literature, three of the 10 crossmatches are in the field of the overdensity at $z = 3.23$: CDFS016526 did not converge with BEAGLE, CDFS013394 and CDFS019446 have sSFR inconsistent with typical values of passive galaxies. Among the members of the overdensity at $z = 3.55$, we identified five candidates: CDFS004503 is consistent with being passive, CDFS005479 and CDFS006294 are AGN, CDFS003718 and CDFS004587 have sSFR inconsistent with typical values of passive galaxies. In overdensity at $z = 3.43$, we discovered two candidates; CDFS019505 is an AGN and CDFS019883 is consistent with being passive.

Importantly, our analysis revealed that some of the passive galaxies from the literature, were actually located within overdensities. This was a significant finding as their presence in overdense regions was not previously known.

Chapter 4

Analysis

4.1 Properties of the overdensities at $3 < z < 4$

For each ovedensity in CDFS and UDS, we report the coordinates of the densest peak, an identification name that will be used along the paper, their maximum volume, and dark matter halo mass (Table 4.1.1). As a volume, we report the cylindrical volume implied by the redshift distribution which is affected by photometric redshift error. As dark matter halo mass, we report the value obtained from the total stellar mass of members and the calibration from van der Burg et al. (2014).

Table 4.1.1: Presents detailed information on the identified protoclusters, including central coordinates, names, volumes, and halo masses.

RA [J2000]	DEC [J2000]	Field	Name	N	Volume [Mpc^3]	Dark Matter Halo [10^{12} M$_\odot$]	AGN	zspec	zphot
53.1346	-27.6954	CDFS	z323	27	8186 ± 614	0.74 [2.33, 0.13]	0	3	24
53.1229	-27.7404	CDFS	z329	31	13 356 ± 581	3.60 [8.69, 0.93]	0	3	28
53.0137	-27.7388	CDFS	z343	10	281 ± 91	14.90 [28.60, 5.44]	2	7	3
53.0985	-27.8060	CDFS	z354	22	5645 ± 871	0.49 [1.63, 0.07]	0	4	18
53.1187	-27.8596	CDFS	z355	82	31 230 ±1974	28.50 [49.30, 12.10]	5	8	74
53.0712	-27.6921	CDFS	z369	18	3184 ± 445	0.54 [1.79, 0.09]	0	5	13
34.2602	-5.2498	UDS	z324	31	5527 ± 829	3.17 [7.81, 0.79]	0	4	27
34.4552	-5.2023	UDS	z327	20	1422 ± 266	1.32 [3.76, 0.27]	0	1	19
34.5203	-5.1648	UDS	z332	29	8015 ± 903	0.69 [2.17, 0.12]	0	4	25
34.4027	-5.1648	UDS	z349	7	139 ± 34	0.13 [0.55, 0.01]	0	1	6
34.3427	-5.2423	UDS	z351	10	1230 ± 131	0.17 [0.67, 0.21]	0	0	10
34.5186	-5.2356	UDS	z365	11	994 ± 164	0.29 [1.07, 0.42]	0	4	7
34.5427	-5.2023	UDS	z369	48	18 090 ±1940	0.78 [16.70, 2.45]	0	5	43
53.0705	-27.8685	CDFS	G-A	39	9938 ± 652	3.09 [7.66, 0.77]	2	5	34
53.1132	-27.8698	CDFS	G-B	25	2915 ± 188	13.60 [26.50, 4.87]	3	3	22
53.1593	-27.8771	CDFS	G-C	16	1803 ± 164	0.84 [2.57, 0.15]	0	0	16

In the analysis of the 13 over-densities, it was observed that only two galaxies

meet the passive criteria. These galaxies are located in protoclusters $z355$ and $z343$ respectively (Fig. 4.1.1). They both exhibit sSFR values consistent with passive galaxies. To complement our analysis, we included a passive galaxy from the field, specifically CDFS013394, located within the $z323$ field. This inclusion provides a broader perspective, contrasting the characteristics of passive galaxies in dense protocluster environments with those in less dense field regions. It is worth noting that the overdensities, which contain passive galaxies, also host AGN. In contrast, the overdensities in UDS present neither passive galaxies nor AGN.

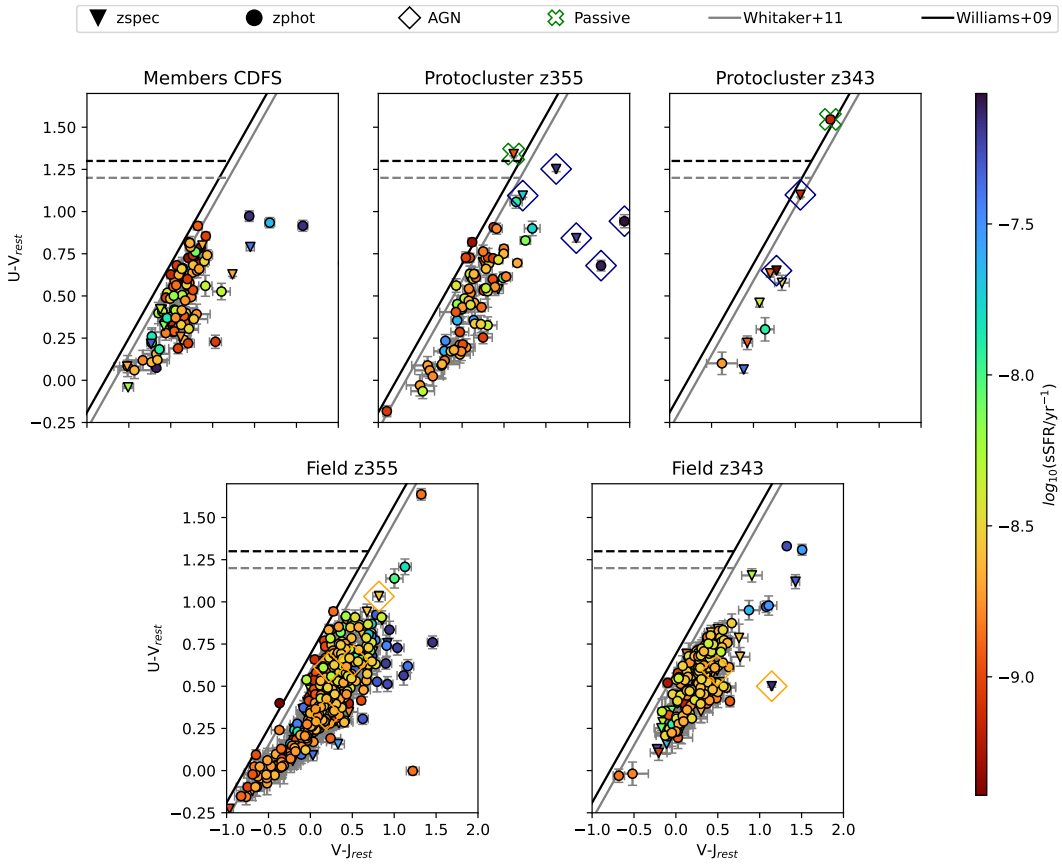

Figure 4.1.1: Multiple UVJ diagrams showcasing galaxies in various conditions. Upper left: member galaxies from protoclusters excluding those with passive galaxies. Upper center: protocluster at z=3.55. Upper right: protocluster at z=3.43. Lower left: field galaxies associated with protocluster z=3.55. Lower right: field galaxies associated with protocluster z=3.43. The color scale denotes log(sSFR), with red signifying lower values and blue higher ones. Different shapes represent the nature of the galaxies: triangles for spectroscopic redshift, dots for photometric redshift, diamonds for AGN, and green crosses for passive galaxies. The lines in the diagrams outline the classification criteria set by Williams et al. (2009) and Whitaker et al. (2011).

4.2 Scaling Relations

Fig. 4.2.1 illustrates the 'main sequence' of star-forming galaxies, that shows a distinct pattern in the relationship between ongoing star formation processes and the galaxy mass within our sample (Santini et al., 2017). Notably, the passive galaxies in our sample are observed to be the most massive. Furthermore, there is a noticeable mass gap between the passive galaxies and other members, highlighting significant differences in both mass and star formation activity. Interestingly, when AGN are excluded from the analysis, the passive galaxies exhibit the highest SFR and stellar mass compared to the other members.

In Fig. 4.2.2, we show the U-V color vs Stellar Mass diagram. It is evident that there is a distinct gap between passive and star-forming galaxies, particularly in terms of color and mass. Passive galaxies are more massive and display redder colors, while star-forming galaxies are characterized by bluer colors and lower mass. This observation is consistent with theoretical expectations and implies specific stellar characteristics for each galaxy type. The redder color of passive galaxies suggests that they host older and cooler stars. Conversely, the bluer color of star-forming galaxies points to the presence of younger and hotter stars, reflecting ongoing star formation processes.

In Fig. 4.2.3, we show the SFR surface density ($\Sigma_{\rm SFR}$) vs stellar mass. The $\Sigma_{\rm SFR}$ was calculated as the Star Formation Rate (SFR) divided by the galaxy's area, determined using the formula πr^2, where r is the half light radius of the galaxy. Passive galaxies exhibit low $\Sigma_{\rm SFR}$ in comparison to the field galaxies. As proposed in Salim et al. (2023), the $\Sigma_{\rm SFR}$–Stellar Mass together with the sSFR-Stellar Mass diagram provide a valuable evolutionary perspective, revealing the level of star formation activity in galaxies. Salim et al. (2023) also emphasize that $\Sigma_{\rm SFR}$, by being tied to molecular gas density and stellar feedback effectiveness, offers a clearer distinction between different galaxy types, including starburst and spheroid-dominated galaxies. This insight supports our analysis, which suggests that the low $\Sigma_{\rm SFR}$ in passive galaxies could be indicative of their evolutionary stage, rather than merely a consequence of their stellar mass.

In Fig. 4.2.4, we present the *Tau* over age ratio (τ) vs *Age*, were τ is SF timescale.

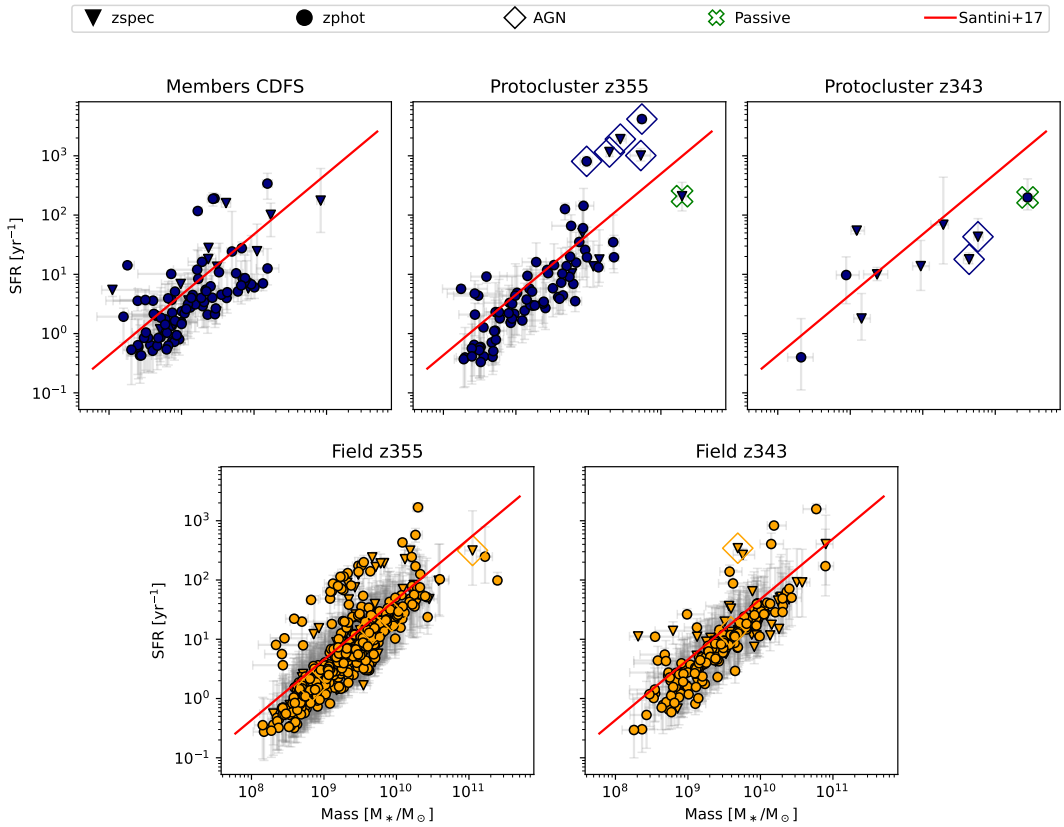

Figure 4.2.1: Star Formation Rate (SFR) plotted against stellar mass for various galaxy samples. Upper left: member galaxies from protoclusters excluding those with passive galaxies. Upper center: protocluster at z=3.55. Upper right: protocluster at z=3.43. Lower left: field galaxies associated with protocluster z=3.55. Lower right: field galaxies associated with protocluster z=3.43. Different symbols represent the nature of the galaxies: triangles for galaxies with spectroscopic redshift, dots for those with photometric redshift, diamonds for AGN, and crosses for passive galaxies.

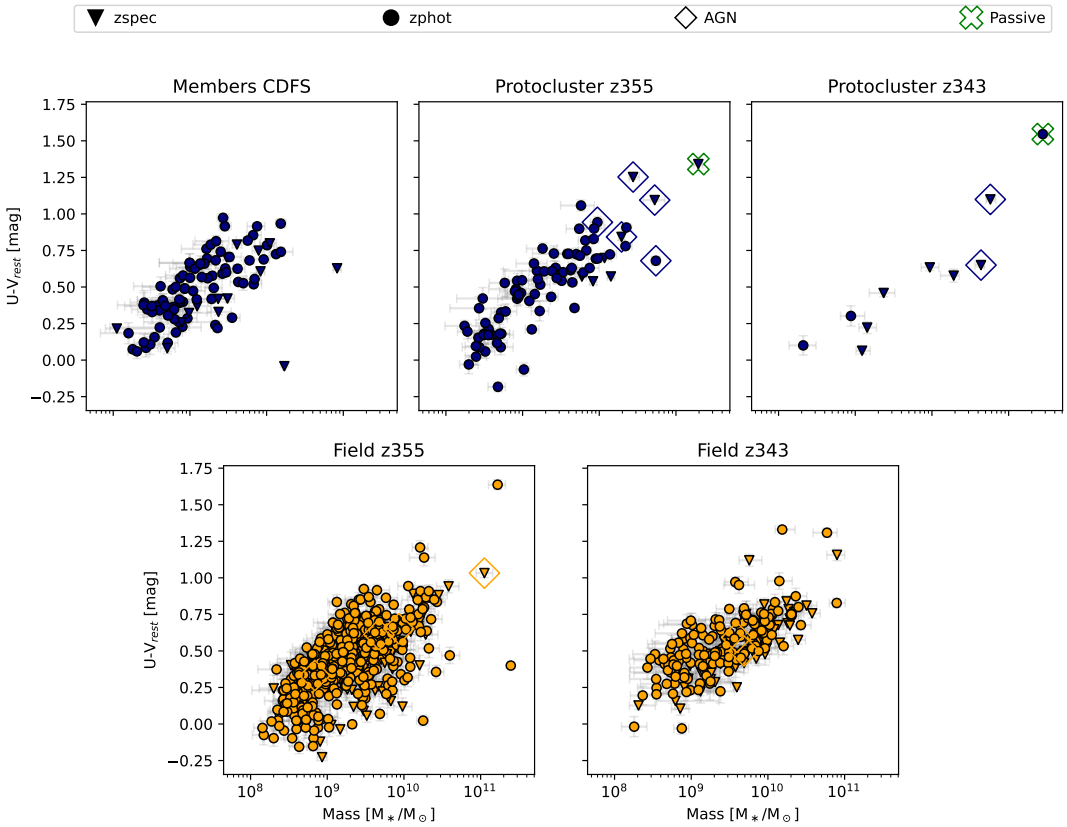

Figure 4.2.2: (U-V) rest frame vs Mass diagrams of galaxies under various conditions. Upper left: member galaxies from protoclusters excluding those with passive galaxies. Upper center: protocluster at z=3.55. Upper right: protocluster at z=3.43. Lower left: field galaxies associated with protocluster z=3.55. Lower right: field galaxies associated with protocluster z=3.43. Different shapes represent the nature of the galaxies: triangles for spectroscopic redshift, dots for photometric redshift, diamonds for AGN, and crosses for passive galaxies.

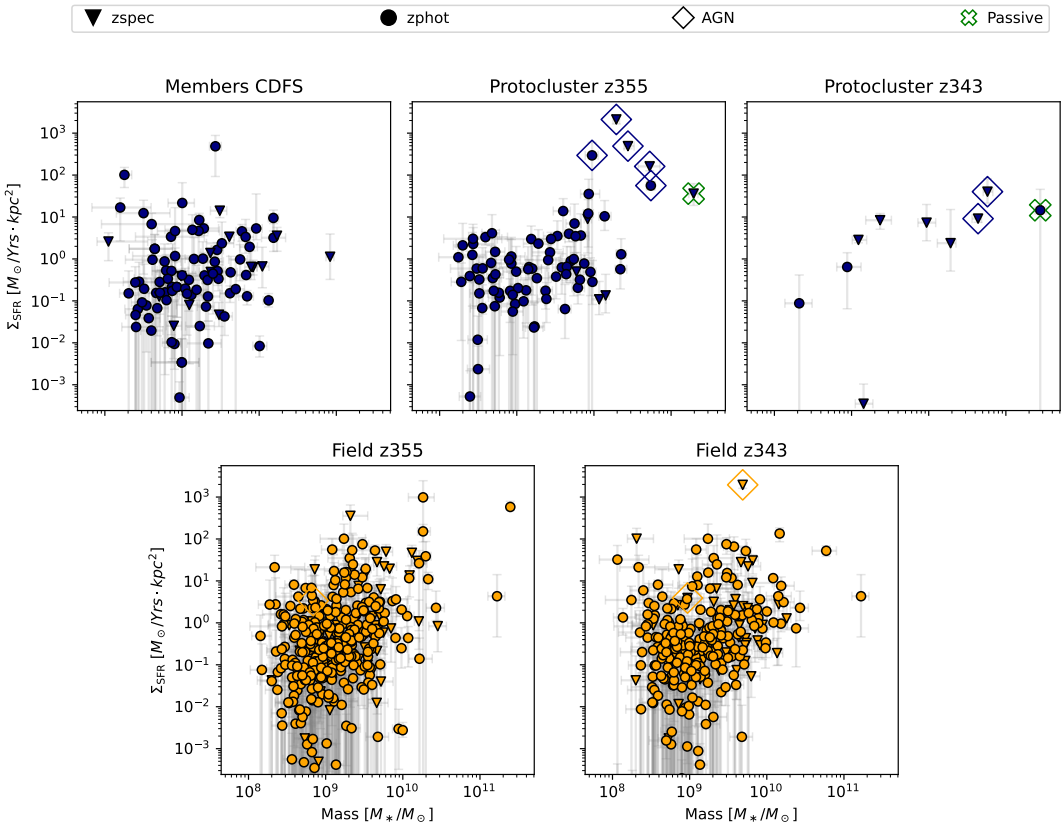

Figure 4.2.3: Surface density SFR vs Mass diagrams of galaxies under various conditions. Upper left: member galaxies from protoclusters excluding those with passive galaxies. Upper center: protocluster at z=3.55. Upper right: protocluster at z=3.43. Lower left: field galaxies associated with protocluster z=3.55. Lower right: field galaxies associated with protocluster z=3.43. Different shapes represent the nature of the galaxies: triangles for spectroscopic redshift, dots for photometric redshift, diamonds for AGN, and crosses for passive galaxies.

If we imagine a line oblique to most of the data, we observe that younger galaxies (characterized by low Age) exhibit higher Tau/Age ratios, indicative of ongoing star formation processes. Conversely, older galaxies (high Age) show lower Tau/Age values, suggesting a quenching phase in star formation. Notably, passive galaxies, which are typically older with respect to the SF episode length, show lower Tau/Age ratios.

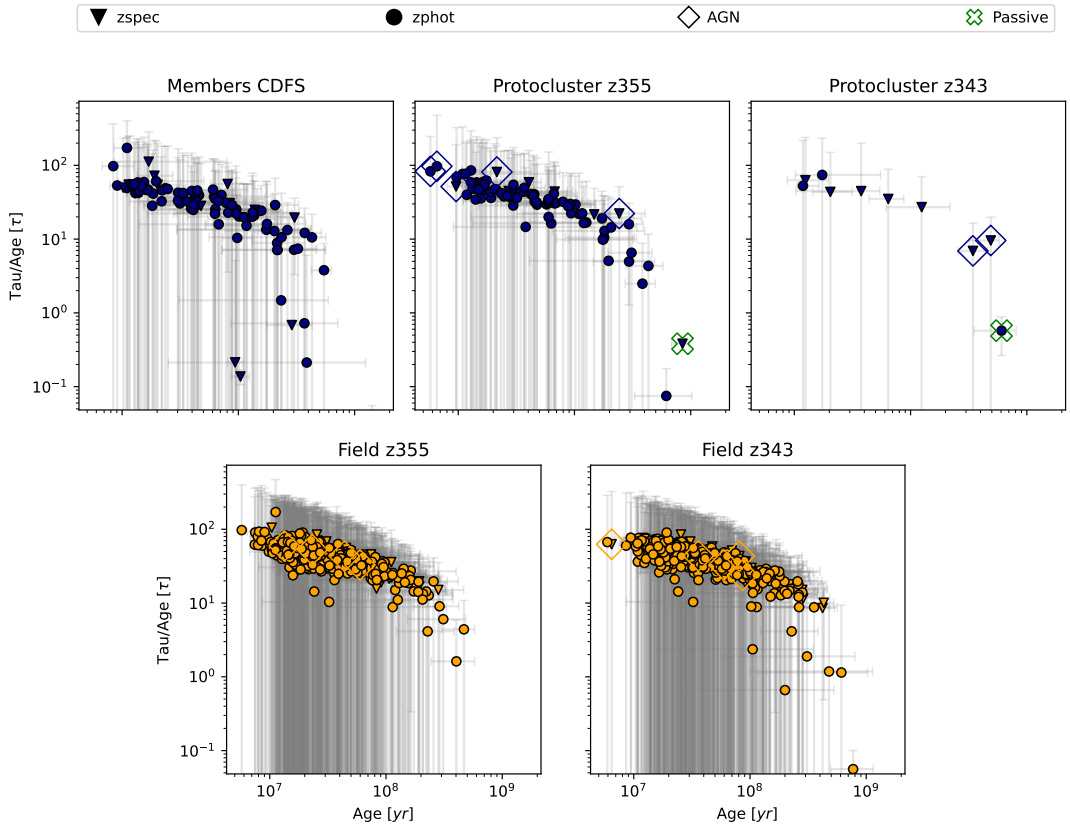

Figure 4.2.4: Tau/Age vs Age diagrams of galaxies under various conditions. Upper left: member galaxies from protoclusters excluding those with passive galaxies. Upper center: protocluster at z=3.55. Upper right: protocluster at z=3.43. Lower left: field galaxies associated with protocluster z=3.55. Lower right: field galaxies associated with protocluster z=3.43. Different shapes represent the nature of the galaxies: triangles for spectroscopic redshift, dots for photometric redshift, diamonds for AGN, and crosses for passive galaxies.

To study the size of the passive galaxies, we analyzed a half light radius vs Mass diagram, as shown in Fig. 4.2.5. We observed that passive galaxies are compact and have a size consistent with early-type galaxies, in line with the findings of van der Wel

et al. (2014).

In the Size vs Mass diagram (Fig. 4.2.5), we note that the majority of field galaxies and members align with late-type characteristics. At redshift 0, this would translate to spiral and irregular galaxies, typically associated with active star formation processes. In contrast, passive galaxies in our sample are consistent with early-type characteristics, corresponding at redshift 0 to elliptical galaxies with low star formation.

The compactness of passive galaxies carries significant implications. It suggests that their Star Formation Rate (SFR) is concentrated in a smaller area. Combining this observation with the fact that these galaxies are also the most massive, we can infer that they possess a high stellar density. In other words, passive galaxies in our sample are not only massive, but this mass is concentrated in a relatively small volume, reflecting an especially efficient and compact evolutionary state.

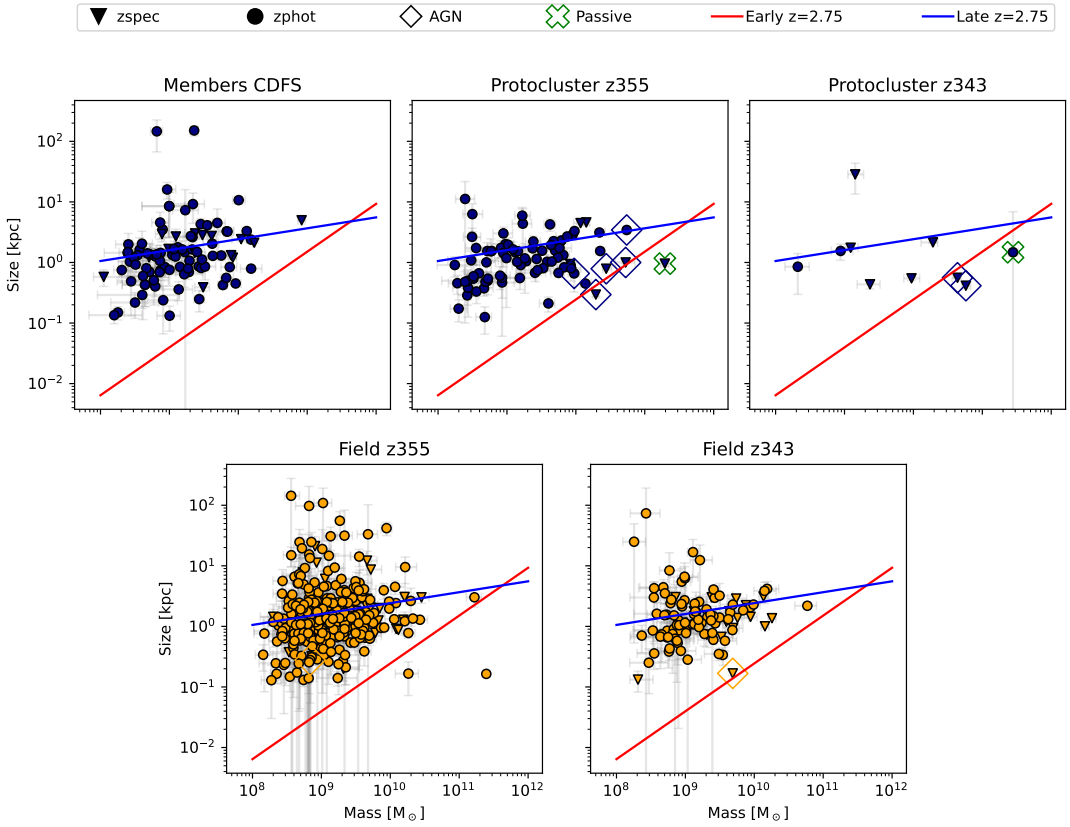

Figure 4.2.5: Size vs Mass diagrams of galaxies under various conditions. Upper left: member galaxies from protoclusters excluding those with passive galaxies. Upper center: protocluster at z=3.55. Upper right: protocluster at z=3.43. Lower left: field galaxies associated with protocluster z=3.55. Lower right: field galaxies associated with protocluster z=3.43. Different shapes represent the nature of the galaxies: triangles for spectroscopic redshift, dots for photometric redshift, diamonds for AGN, and crosses for passive galaxies. The lines on the diagram are based on the criteria set by van der Wel et al. (2014)

Chapter 5

Discussion

Our research endeavors to elucidate the evolutionary trajectories of galaxies within protoclusters, focusing on qualitative understanding and comparison with simulations. By employing the BEAGLE tool for spectral energy distribution (SED) fitting and utilizing data from the VANDELS survey, we aim to unravel the complexities of galaxy evolution in dense environments. This multifaceted approach facilitates a nuanced comprehension of the factors influencing galaxy evolution in protoclusters.

In examining the two overdensities containing passive galaxies, $z355$ and $z343$, our findings indicate significant distinctions compared to other observed groups. These overdensities are characterized by passive galaxies with redder coloration, higher mass, and the frequent presence of AGNs.

When compared to the simulations outlined in Chiang et al. (2013), these observations suggest that the Dark Matter Halo sizes are consistent with those expected in a protocluster setting. The variances we observe encompass not only color and mass but also an older stellar age and distinct sSFR-Mass and Σ_{SFR}-Mass ratios, aligning with the typical attributes of passive galaxies.

Our analysis, based on the SF timescale (τ) and the age of the galaxy, has led to the estimation of key epochs in the history of passive galaxies within the overdensities. Given the delayed star formation history model, for the passive galaxy in $z355$, we estimate the onset of formation at $z \sim 6.20$, with the decreasing of star formation already occurring at $z < 4.3$. For $z343$, the formation of the passive galaxy is

traced back to $z \sim 4.8$, with the decrease of star formation occurring at $z < 3.5$.

In Fig. 5.0.1a, we compare the environment around the passive galaxies we found in overdensities with that around the passive galaxy from the literature in the field. We show the number of galaxies as a function of the distance from the passive galaxies. At a distance of 100 ckpc, more than two galaxies are observed surrounding the passive galaxies in the $z355$ and $z343$ overdensities, whereas none are found around the passive galaxy in the field.

We conducted a Kolmogorov-Smirnov (KS) test to quantify the environmental differences within the first 300 cKpc in the overdensities and in the field. The KS test results for $z355$ compared to $z343$ yielded a statistic of 0.2 with a p-value of 0.182, suggesting a moderate difference. Comparing $z323$ with $z343$, the KS statistic was 0.767 with a p-value of 1.39×10^{-17}, and for $z323$ compared to $z355$, the statistic was 0.883 with a p-value of 1.23×10^{-24}. These results indicate that the distribution of galaxies around passive galaxies in the overdensities and in the field are drawn from significantly different distributions, highlighting distinct environmental influences.

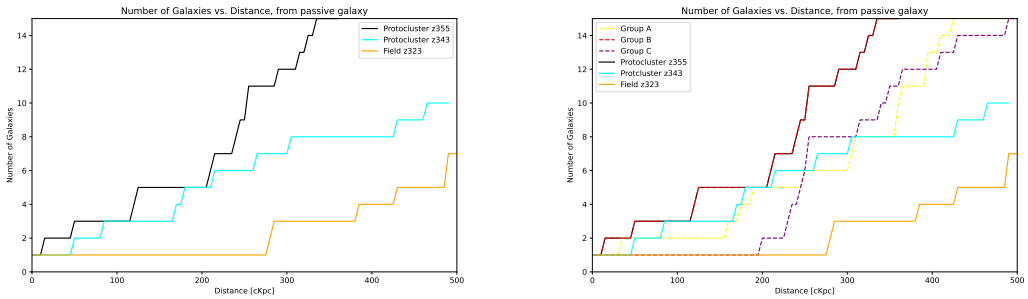

(a) Overdensties **(b)** Group Differentiation

Figure 5.0.1: Spatial Distribution of Galaxy Counts in Overdensities. **Left:** Distribution relative to the passive galaxy ($z343$ in cyan, $z355$ in black, $z323$ in orange). **Right:** Distribution showing distinct groups within the overdensities (Groups A, B, C differentiated by dashed lines). These visualizations collectively depict the spatial dynamics and group formations around passive galaxies in various cosmic environments.

5.1 Overdensity $z355$

In our investigation of the z355 overdensity, a critical aspect was to explore the spatial distribution of galaxies within this region. In Fig. 5.1.1, we present the analysis of the RA and DEC coordinates of galaxies in z355, incorporating kernel density estimations to enhance our understanding of their spatial arrangement. This analysis was performed in the context that the z355 overdensity has a large redshift range.

Therefore, by employing kernel density estimations along the RA and DEC axes (Fig. 5.1.1), we observed three distinct concentrations of galaxies, particularly along the RA axis, within the z355 overdensity. This led us to subdivide the galaxies within the overdensity into three distinct groups, thereby providing a clearer insight into the variations in galaxy concentration and distribution across different segments of the protocluster. In Fig. 5.1.2a, we include the additional passive galaxies identified from the literature, further enriching our understanding of the galactic composition within these groups.

For clarity, these concentrations are defined and color-coded, in Fig. 5.1.2a where our passive galaxy is located. As we move from the right to the left on the diagram, these groups reveal the underlying structural features of the overdensity. Furthermore, Fig. 5.1.2b presents the redshift distribution of the three groups, where distinct peaks can be observed. Specifically, a peak at redshift $z \sim 3.55$ is associated with Group B, and another at $z \sim 3.7$ is identified with Group A. Also, Shah et al. (2023) identified six massive protostructures within the redshift range of $2.5 < z < 4.5$ in ECDFS, using public and proprietary spectroscopic data in addition to photometric redshifts. Our Group A overlaps with a massive structure at $z \approx 3.69$ (S5 structure from Tab1 in Shah et al. (2023)). Our Group B overlaps with a less massive structure at $z = 3.58$ (Shah et al. private communication).

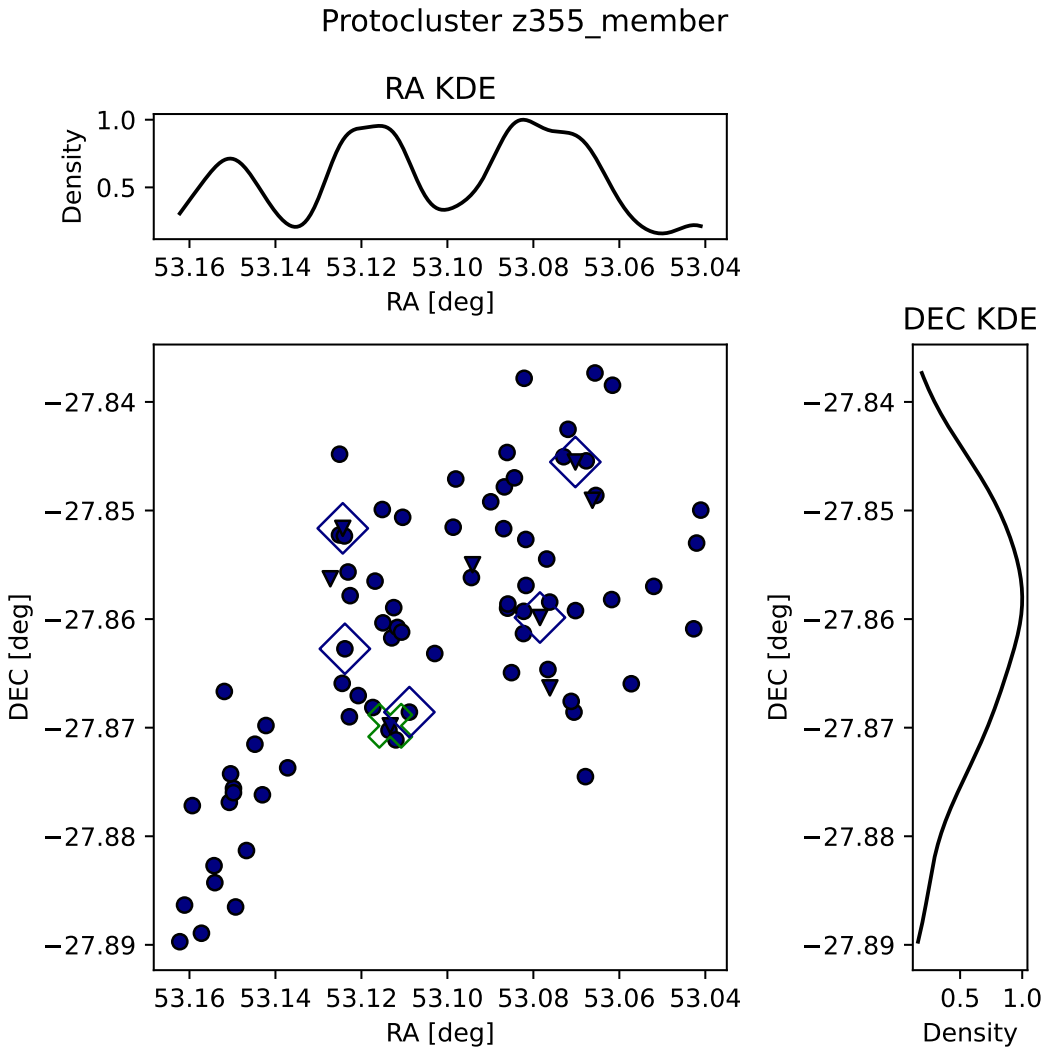

Figure 5.1.1: Spatial Distribution and Kernel Density Estimations of the z355 Overdensity. The central plot displays the RA and DEC scatter plot, illustrating the spatial distribution of galaxies within the z355 overdensity. The galaxies are represented with different symbols based on their redshift types: circles for photometric redshift and downward triangles for spectroscopic redshift. Additionally, AGNs are denoted by diamonds. On the margins, kernel density estimations are presented: to the right for DEC, and at the top for RA. These density estimations provide an intuitive view of the concentration and dispersion of galaxies along each axis, highlighting the distinct spatial characteristics and the AGN distribution within the z355 overdensity.

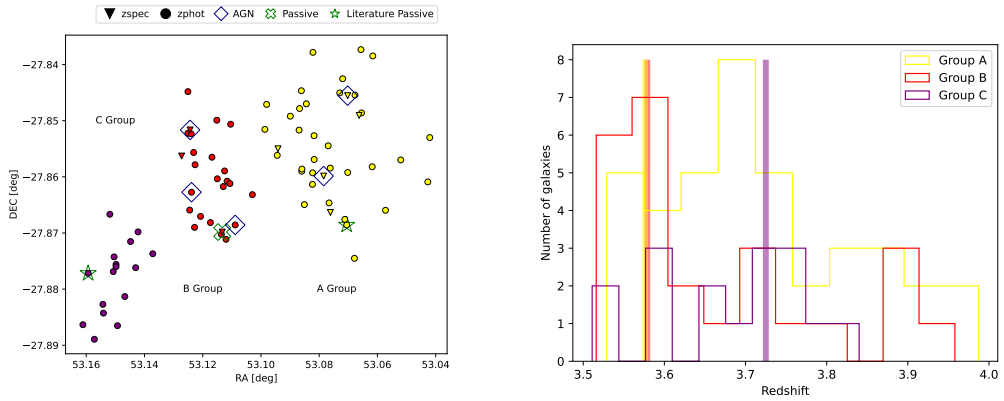

(a) RA and DEC Distribution of Galaxies in the $z355$ Overdensity.

(b) Redshift Distribution Histogram for the Groups in $z355$

Figure 5.1.2: Comprehensive Spatial and Redshift Analysis of the z355 Overdensity. **Left:** The RA-DEC distribution of galaxies showcases the spatial segregation of groups A (yellow), B (red), and C (purple) within z355, using distinct symbols to represent photometric redshifts (circles), spectroscopic redshifts (downward triangles), AGNs (diamonds), and passive galaxies (crosses in green, with green stars marking those identified in previous literature). **Right:** The redshift distribution histogram for each group in the z355 overdensity, highlighting how each group's composition varies across redshifts. Vertical lines in the histogram represent the redshifts at which the passive galaxies in each group are located, with colors corresponding to their respective groups.

5.2 Overdensity $z343$

In Fig. 5.0.1b and Fig. 5.0.1a, we show number of galaxies arround the passive galaxy in the $z343$ overdensity. Notably, this environment, while not being the densest, is denser than that of the passive galaxy in the field of $z323$. Furthermore, the redshift range of the $z343$ overdensity is considerably narrower than that of the $z355$ overdensity, indicating a more concentrated galaxy distribution in $z343$.

5.3 Comparison with Previous Studies

In Fig. 5.3.1, we compare the age and mass of the members of our overdensities in CDFS and the passive galaxies from the literature. The green points denote our identified passive galaxies, which align closely in terms of age and mass with passive galaxies reported in the literature. Also, they are among the most massive passive galaxies. We can see that, the star forming members are younger and less massive than

the passive galaxies.

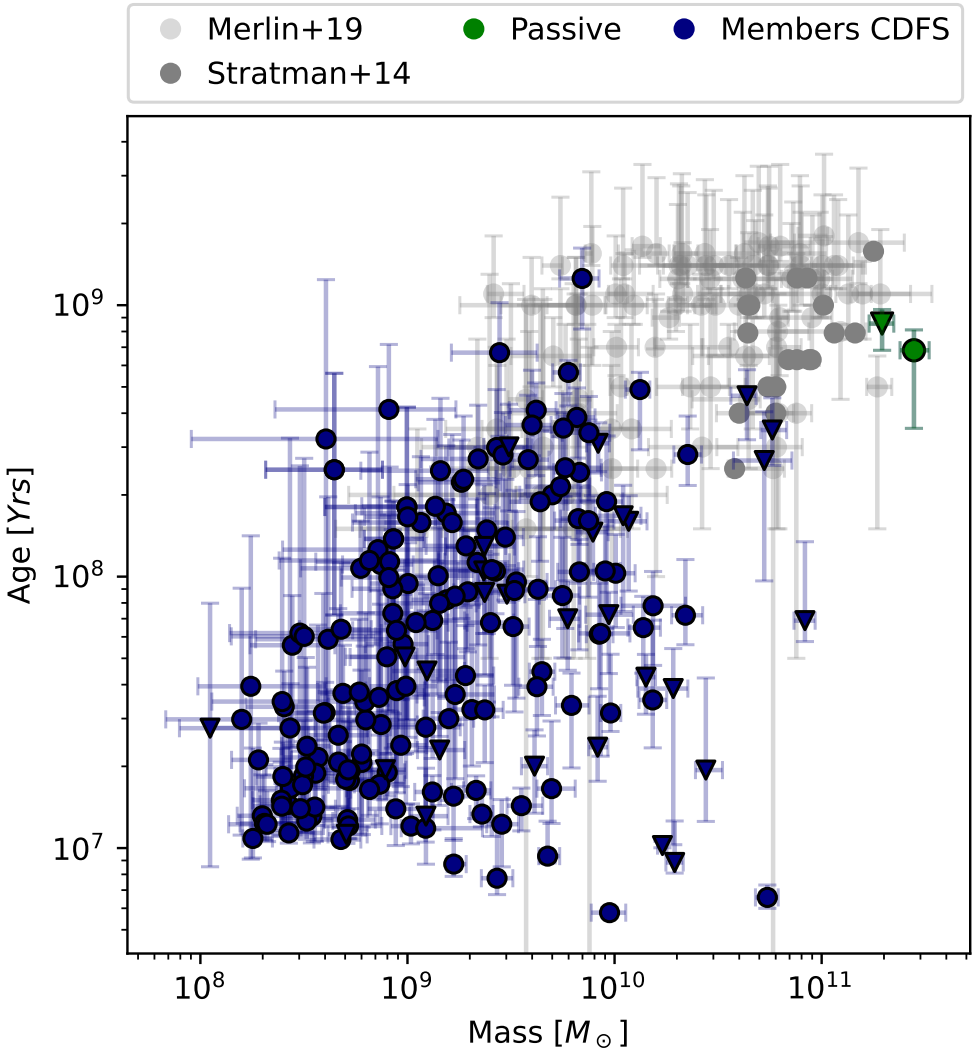

Figure 5.3.1: Age vs Mass diagram. Navy points represent members of protoclusters in CDFS. Green points denote passive galaxies. Light gray points correspond to passive galaxies from Merlin et al. (2019), while dark gray points represent passive galaxies from Straatman et al. (2014).

5.4 Comparison with TNG300

Our analysis of the evolutionary trajectories of galaxies within protoclusters at different redshifts was significantly enhanced by the use of the TNG300 simulation. This process involved several critical steps, which are detailed below:

5.4.1 Accessing TNG300 Simulation Data

Initially, I created an account on the TNG project website and requested access to the TNG300 simulation data. This was a crucial step as it provided me with the necessary resources to conduct my research effectively.

5.4.2 Learning to Work with TNG Data

I gained proficiency in working with TNG data under the guidance of Professor Maria Celeste Artale. Her expertise was instrumental in helping me understand the complexities of the simulation data and how to manipulate it for my research needs.

5.4.3 Selection of Protoclusters

One of the pivotal aspects of the study was the selection of protoclusters with Dark Matter Halos consistent with those observed in our overdensities containing passive galaxies. This selection process was guided by Professor Artale's insights and expertise, ensuring that the chosen protoclusters were relevant and comparable to our observational data.

5.4.4 Programming for Data Extraction

To analyze the selected protoclusters, I developed a Python program capable of extracting merger trees of the galaxies within these structures. This program was designed to sift through the extensive data of the TNG300 simulation, focusing on the key aspects relevant to our study, such as passive galaxy fractions and their evolution across various redshifts.

5.4.5 Analysis of Passive Galaxies Across Redshifts

Using the Python program, I conducted a detailed analysis of the passive galaxies within the selected protoclusters. This involved studying their specific star formation rates (sSFR) at various redshifts ($z = 3$, $z = 2$, $z = 1$, and $z = 0.6$), following the criteria set

by Carnall et al. (2018a). This enabled us to estimate the fraction of passive galaxies at these different epochs and to understand their evolutionary patterns in the context of the TNG300 simulation.

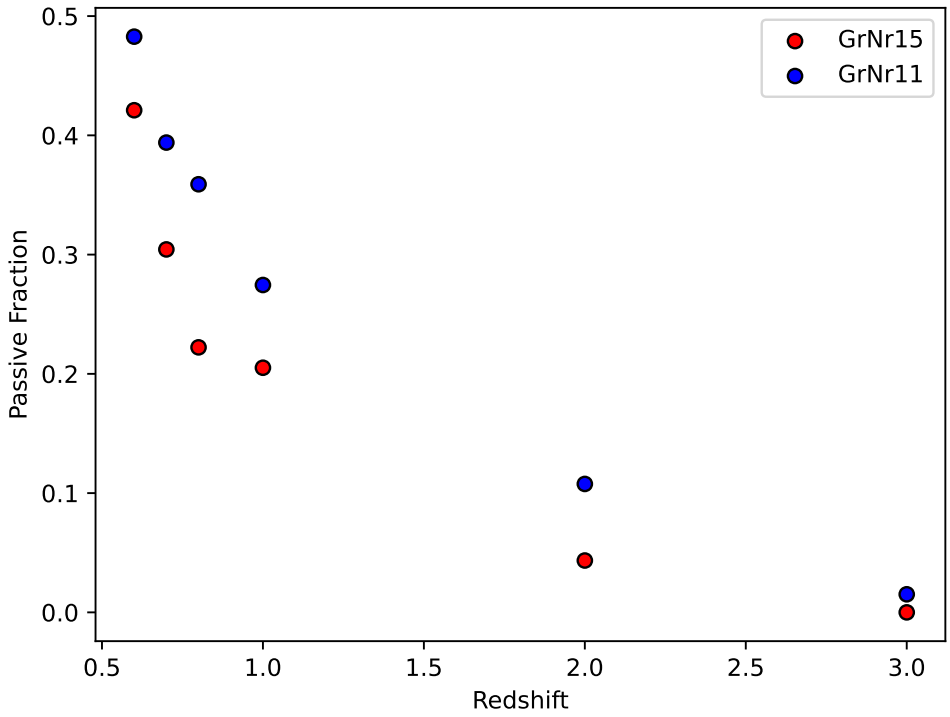

Figure 5.4.1: Passive Galaxy Fraction as a Function of Redshift. This graph illustrates the evolutionary trend in the fraction of passive galaxies across different redshifts. Red points denote data for cluster GrNr15, while blue points represent cluster GrNr11. The analysis underscores the influence of early passive galaxy formation in cluster GrNr11.

The results of this comprehensive analysis are presented in Figure 5.4.1, which highlights the distinct trajectories in the development of passive galaxies within these two clusters, emphasizing the significance of early passive galaxy formation in the evolution of protocluster structures.

Chapter 6

Conclusion

In this work, we studied the characteristics and the distribution of the galaxies within 13 overdensities identified at $3 < z < 4$. Our key findings can be summarized as follows:

- Among the 13 overdensities, only two were found to contain passive galaxies (Fig. 4.1.1). This highlights the rarity of such galaxies in these dense environments.

- The passive galaxies identified in the overdensities are redder and more massive compared to other overdensity members (Fig. 4.2.2).

- Our results indicate that passive galaxies in our sample have consistent with early-type galaxies (Fig. 4.2.5), further supporting their classification as passive.

- The data trend in Figure 4.2.4 clearly suggests that passive galaxies possess both lower τ values and greater age, distinguishing them from the broader galaxy population.

- In the case of overdensity $z355$, a broader redshift range was observed compared to other overdensities. We further subdivided $z355$ into three groups based on a kernel density estimation (KDE) test (Fig. 5.1.1), revealing that the passive galaxy is located in the highest density peak within this overdensity.

- The presence of passive galaxies in our study aligns with previous research, lending further credibility to our results and underscoring the robustness of our analysis.

- A noteworthy observation is the detection of AGNs exclusively in overdensities that contain passive galaxies, suggesting a potential link between AGN activity and the presence of passive galaxies in these environments.

- As observed in Figure 5.0.1, the passive galaxy in $z355$ is situated in a region of higher overdensity compared to $z343$. Furthermore, within the different groups of $z355$, it is located in the central group, which is the area of highest density. A Kolmogorov-Smirnov (KS) test was performed, revealing that the environments of the passive galaxies in $z355$, $z343$, and $z323$ do not originate from the same distribution, and that passive galaxies are located in the highest density peaks of the overdensities.

- In our investigation into galaxy evolution within the observed overdensities, we engaged in a thorough analysis of the specific star formation rates (sSFR) and stellar mass accumulation in z=3 protoclusters, as depicted in the TNG300 simulation. This study concentrated on two contrasting protoclusters: GrNr11, which incorporates a passive galaxy, and GrNr15, characterized exclusively by star-forming galaxies. Remarkably, we found that the sSFR in the passive galaxy of GrNr11 remained significantly elevated until reaching $z = 6$, subsequently experiencing a steep decline. This was accompanied by a considerable surge in stellar mass from $z = 6$ to $z = 3$, suggesting a parallel in the evolutionary paths of passive galaxies in our studied overdensities. Furthermore, our analysis, in alignment with the TNG300 simulation, uncovered a noteworthy trend: the fraction of passive galaxies in GrNr11 was about 10% higher than that in GrNr15 as of $z = 0.6$. This variance in the proportion of passive galaxies, as showcased in Figure 5.4.1, elucidates the vital role played by the early presence of passive galaxies in shaping the evolutionary trajectories of galaxies within protoclusters.

- Finally, the estimated Dark Matter Halo values for $z355$ and $z343$ are in line with

those expected for protoclusters, as per the simulations by Chiang et al. (2013).

In conclusion, our study elucidated the evolution of galaxies within $z = 3 - 4$ overdensities. Key insights include the rarity of passive galaxies in dense environments, their distinct properties of being redder and more massive, and their concentration at the highest density peaks. Spatial analysis revealed a correlation between AGN presence and passive galaxies. Furthermore, overdensities containing passive galaxies at high redshifts showed a higher fraction of such galaxies at lower redshifts, offering new perspectives on environmental impacts on galactic evolution and early universe structure formation.

Bibliography

Balogh, M. L., Morris, S. L., Yee, H. K. C., Carlberg, R. G., and Ellingson, E. (1999). Differential Galaxy Evolution in Cluster and Field Galaxies at z_0.3. , 527(1):54–79.

Behroozi, P. S., Wechsler, R. H., and Conroy, C. (2013). The Average Star Formation Histories of Galaxies in Dark Matter Halos from z = 0-8. , 770(1):57.

Calabrò, A., Pentericci, L., Talia, M., Cresci, G., Castellano, M., Belfiori, D., Mascia, S., Zamorani, G., Amorín, R., Fynbo, J. P. U., Ginolfi, M., Guaita, L., Hathi, N. P., Koekemoer, A., Llerena, M., Mannucci, F., Santini, P., Saxena, A., and Schaerer, D. (2022). Properties of the interstellar medium in star-forming galaxies at redshifts $2 \leq z \leq 5$ from the VANDELS survey. , 667:A117.

Carnall, A. C., McLure, R. J., Dunlop, J. S., Cullen, F., McLeod, D. J., Wild, V., Johnson, B. D., Appleby, S., Davé, R., Amorin, R., Bolzonella, M., Castellano, M., Cimatti, A., Cucciati, O., Gargiulo, A., Garilli, B., Marchi, F., Pentericci, L., Pozzetti, L., Schreiber, C., Talia, M., and Zamorani, G. (2019). The VANDELS survey: the star-formation histories of massive quiescent galaxies at $1.0 < z < 1.3$. , 490(1):417–439.

Carnall, A. C., McLure, R. J., Dunlop, J. S., and Davé, R. (2018a). Inferring the star formation histories of massive quiescent galaxies with BAGPIPES: evidence for multiple quenching mechanisms. , 480(4):4379–4401.

Carnall, A. C., McLure, R. J., Dunlop, J. S., and Davé, R. (2018b). Inferring the star formation histories of massive quiescent galaxies with BAGPIPES: evidence for multiple quenching mechanisms. , 480(4):4379–4401.

Castellano, M., Belfiori, D., Pentericci, L., Calabrò, A., Mascia, S., Napolitano, L., Caro, F., Charlot, S., Chevallard, J., Curtis Lake, E., Talia, M., Bongiorno, A., Fontana, A., Fynbo, J. P. U., Garilli, B., Guaita, L., McLure, R. J., Merlin, E., Mignoli, M., Moresco, M., Pompei, E., Pozzetti, L., Saldana Lopez, A., Saxena, A., Santini, P., Schaerer, D., Schreiber, C., Shapley, A. E., Vanzella, E., and Zamorani, G. (2023). The ionizing photon production efficiency of bright $z \sim 2 - 5$ galaxies. , 675:A121.

Chevallard, J. and Charlot, S. (2016). Modelling and interpreting spectral energy distributions of galaxies with BEAGLE. , 462(2):1415–1443.

Chiang, Y.-K., Overzier, R., and Gebhardt, K. (2013). Ancient Light from Young Cosmic Cities: Physical and Observational Signatures of Galaxy Proto-clusters. , 779(2):127.

Collins, M. L. M. and Read, J. I. (2022). Observational constraints on stellar feedback in dwarf galaxies. *Nature Astronomy*, 6:647–658.

Dekel, A. and Birnboim, Y. (2008). Gravitational quenching in massive galaxies and clusters by clumpy accretion. , 383(1):119–138.

Dressler, A., Oemler, Augustus, J., Couch, W. J., Smail, I., Ellis, R. S., Barger, A., Butcher, H., Poggianti, B. M., and Sharples, R. M. (1997). Evolution since z = 0.5 of the Morphology-Density Relation for Clusters of Galaxies. , 490(2):577–591.

Ebeling, H., Edge, A. C., and Henry, J. P. (2001). MACS: A Quest for the Most Massive Galaxy Clusters in the Universe. , 553(2):668–676.

Fabian, A. C. (2012). Observational Evidence of Active Galactic Nuclei Feedback. , 50:455–489.

Feldmann, R. and Mayer, L. (2015). The Argo simulation - I. Quenching of massive galaxies at high redshift as a result of cosmological starvation. , 446(2):1939–1956.

Garilli, B., McLure, R., Pentericci, L., Franzetti, P., Gargiulo, A., Carnall, A., Cucciati, O., Iovino, A., Amorin, R., Bolzonella, M., Bongiorno, A., Castellano, M., Cimatti, A., Cirasuolo, M., Cullen, F., Dunlop, J., Elbaz, D., Finkelstein, S., Fontana, A., Fontanot, F., Fumana, M., Guaita, L., Hartley, W., Jarvis, M., Juneau, S., Maccagni, D., McLeod, D., Nandra, K., Pompei, E., Pozzetti, L., Scodeggio, M., Talia, M., Calabrò, A., Cresci, G., Fynbo, J. P. U., Hathi, N. P., Hibon, P., Koekemoer, A. M., Magliocchetti, M., Salvato, M., Vietri, G., Zamorani, G., Almaini, O., Balestra, I., Bardelli, S., Begley, R., Brammer, G., Bell, E. F., Bowler, R. A. A., Brusa, M., Buitrago, F., Caputi, C., Cassata, P., Charlot, S., Citro, A., Cristiani, S., Curtis-Lake, E., Dickinson, M., Fazio, G., Ferguson, H. C., Fiore, F., Franco, M., Georgakakis, A., Giavalisco, M., Grazian, A., Hamadouche, M., Jung, I., Kim, S., Khusanova, Y., Le Fèvre, O., Longhetti, M., Lotz, J., Mannucci, F., Maltby, D., Matsuoka, K., Mendez-Hernandez, H., Mendez-Abreu, J., Mignoli, M., Moresco, M., Nonino, M., Pannella, M., Papovich, C., Popesso, P., Roberts-Borsani, G., Rosario, D. J., Saldana-Lopez, A., Santini, P., Saxena, A., Schaerer, D., Schreiber, C., Stark, D., Tasca, L. A. M., Thomas, R., Vanzella, E., Wild, V., Williams, C., and Zucca, E. (2021). The VANDELS ESO public spectroscopic survey. Final data release of 2087 spectra and spectroscopic measurements. , 647:A150.

Giovanelli, R., Haynes, M. P., Kent, B. R., Perillat, P., Saintonge, A., Brosch, N., Catinella, B., Hoffman, G. L., Stierwalt, S., Spekkens, K., Lerner, M. S., Masters, K. L., Momjian, E., Rosenberg, J. L., Springob, C. M., Boselli, A., Charmandaris, V., Darling, J. K., Davies, J., Garcia Lambas, D., Gavazzi, G., Giovanardi, C., Hardy, E., Hunt, L. K., Iovino, A., Karachentsev, I. D., Karachentseva, V. E., Koopmann, R. A., Marinoni, C., Minchin, R., Muller, E., Putman, M., Pantoja, C., Salzer, J. J., Scodeggio, M., Skillman, E., Solanes, J. M., Valotto, C., van Driel, W., and van Zee,

L. (2005). The Arecibo Legacy Fast ALFA Survey. I. Science Goals, Survey Design, and Strategy. , 130(6):2598–2612.

Guaita, L., Pompei, E., Castellano, M., Pentericci, L., Cucciati, O., Zamorani, G., Zoldan, A., Fontanot, F., Bauer, F. E., Amorin, R., Bolzonella, M., de Lucia, G., Gargiulo, A., Hathi, N. P., Hibon, P., Hirschmann, M., Koekemoer, A. M., McLure, R., Pozzetti, L., Talia, M., Thomas, R., and Xie, L. (2020). The VANDELS survey: Discovery of massive overdensities of galaxies at z > 2. Location of Lyα-emitting galaxies with respect to environment. , 640:A107.

Gunn, J. E. and Gott, J. Richard, I. (1972). On the Infall of Matter Into Clusters of Galaxies and Some Effects on Their Evolution. , 176:1.

Gutkin, J., Charlot, S., and Bruzual, G. (2016). Modelling the nebular emission from primeval to present-day star-forming galaxies. , 462(2):1757–1774.

Hopkins, P. F., Quataert, E., and Murray, N. (2012). The structure of the interstellar medium of star-forming galaxies. , 421(4):3488–3521.

Johansson, P. H., Naab, T., and Ostriker, J. P. (2009). Gravitational Heating Helps Make Massive Galaxies Red and Dead. , 697(1):L38–L43.

Kim, K., Malhotra, S., Rhoads, J. E., Joshi, B., Fererras, I., and Pasquali, A. (2018). Galaxy Structure, Stellar Populations, and Star Formation Quenching at $0.6 \lesssim z \lesssim 1.2$. , 867(2):118.

Kocevski, D. D., Hasinger, G., Brightman, M., Nandra, K., Georgakakis, A., Cappelluti, N., Civano, F., Li, Y., Li, Y., Aird, J., Alexander, D. M., Almaini, O., Brusa, M., Buchner, J., Comastri, A., Conselice, C. J., Dickinson, M. A., Finoguenov, A., Gilli, R., Koekemoer, A. M., Miyaji, T., Mullaney, J. R., Papovich, C., Rosario, D., Salvato, M., Silverman, J. D., Somerville, R. S., and Ueda, Y. (2018). VizieR Online Data Catalog: The Chandra UDS survey (X-UDS) (Kocevski+, 2018). *VizieR Online Data Catalog*, page J/ApJS/236/48.

Lu, S., Fang, G., Gu, Y., Yuan, Q., Cai, Z.-Y., and Kong, X. (2021). The Effect of the Morphological Quenching Mechanism on Star Formation Activity at 0.5 < z < 1.5 in 3D-HST/CANDELS. , 913(2):81.

Luo, B., Brandt, W. N., Xue, Y. Q., Lehmer, B., Alexander, D. M., Bauer, F. E., Vito, F., Yang, G., Basu-Zych, A. R., Comastri, A., Gilli, R., Gu, Q. S., Hornschemeier, A. E., Koekemoer, A., Liu, T., Mainieri, V., Paolillo, M., Ranalli, P., Rosati, P., Schneider, D. P., Shemmer, O., Smail, I., Sun, M., Tozzi, P., Vignali, C., and Wang, J. X. (2017). The Chandra Deep Field-South Survey: 7 Ms Source Catalogs. , 228(1):2.

McLure, R. J., Pentericci, L., Cimatti, A., Dunlop, J. S., Elbaz, D., Fontana, A., Nandra, K., Amorin, R., Bolzonella, M., Bongiorno, A., Carnall, A. C., Castellano, M., Cirasuolo, M., Cucciati, O., Cullen, F., De Barros, S., Finkelstein, S. L., Fontanot, F., Franzetti, P., Fumana, M., Gargiulo, A., Garilli, B., Guaita, L., Hartley, W. G., Iovino, A., Jarvis, M. J., Juneau, S., Karman, W., Maccagni, D., Marchi, F., Mármol-Queraltó, E., Pompei, E., Pozzetti, L., Scodeggio, M., Sommariva, V., Talia, M.,

Almaini, O., Balestra, I., Bardelli, S., Bell, E. F., Bourne, N., Bowler, R. A. A., Brusa, M., Buitrago, F., Caputi, K. I., Cassata, P., Charlot, S., Citro, A., Cresci, G., Cristiani, S., Curtis-Lake, E., Dickinson, M., Fazio, G. G., Ferguson, H. C., Fiore, F., Franco, M., Fynbo, J. P. U., Galametz, A., Georgakakis, A., Giavalisco, M., Grazian, A., Hathi, N. P., Jung, I., Kim, S., Koekemoer, A. M., Khusanova, Y., Le Fèvre, O., Lotz, J. M., Mannucci, F., Maltby, D. T., Matsuoka, K., McLeod, D. J., Mendez-Hernandez, H., Mendez-Abreu, J., Mignoli, M., Moresco, M., Mortlock, A., Nonino, M., Pannella, M., Papovich, C., Popesso, P., Rosario, D. P., Salvato, M., Santini, P., Schaerer, D., Schreiber, C., Stark, D. P., Tasca, L. A. M., Thomas, R., Treu, T., Vanzella, E., Wild, V., Williams, C. C., Zamorani, G., and Zucca, E. (2018). The VANDELS ESO public spectroscopic survey. , 479(1):25–42.

Menanteau, F., Sifón, C., Barrientos, L. F., Battaglia, N., Bond, J. R., Crichton, D., Das, S., Devlin, M. J., Dicker, S., Dünner, R., Gralla, M., Hajian, A., Hasselfield, M., Hilton, M., Hincks, A. D., Hughes, J. P., Infante, L., Kosowsky, A., Marriage, T. A., Marsden, D., Moodley, K., Niemack, M. D., Nolta, M. R., Page, L. A., Partridge, B., Reese, E. D., Schmitt, B. L., Sievers, J., Spergel, D. N., Staggs, S. T., Switzer, E., and Wollack, E. J. (2013). The Atacama Cosmology Telescope: Physical Properties of Sunyaev-Zel'dovich Effect Clusters on the Celestial Equator. , 765(1):67.

Merlin, E., Fortuni, F., Torelli, M., Santini, P., Castellano, M., Fontana, A., Grazian, A., Pentericci, L., Pilo, S., and Schmidt, K. B. (2019). Red and dead CANDELS: massive passive galaxies at the dawn of the Universe. , 490(3):3309–3328.

Olsen, L. F., Benoist, C., Cappi, A., Maurogordato, S., Mazure, A., Slezak, E., Adami, C., Ferrari, C., and Martel, F. (2007). Galaxy clusters in the CFHTLS. First matched filter candidate catalogue of the Deep fields. , 461(1):81–93.

Overzier, R. A. (2016). The realm of the galaxy protoclusters. A review. , 24(1):14.

Peng, Y.-j., Lilly, S. J., Kovač, K., Bolzonella, M., Pozzetti, L., Renzini, A., Zamorani, G., Ilbert, O., Knobel, C., Iovino, A., Maier, C., Cucciati, O., Tasca, L., Carollo, C. M., Silverman, J., Kampczyk, P., de Ravel, L., Sanders, D., Scoville, N., Contini, T., Mainieri, V., Scodeggio, M., Kneib, J.-P., Le Fèvre, O., Bardelli, S., Bongiorno, A., Caputi, K., Coppa, G., de la Torre, S., Franzetti, P., Garilli, B., Lamareille, F., Le Borgne, J.-F., Le Brun, V., Mignoli, M., Perez Montero, E., Pello, R., Ricciardelli, E., Tanaka, M., Tresse, L., Vergani, D., Welikala, N., Zucca, E., Oesch, P., Abbas, U., Barnes, L., Bordoloi, R., Bottini, D., Cappi, A., Cassata, P., Cimatti, A., Fumana, M., Hasinger, G., Koekemoer, A., Leauthaud, A., Maccagni, D., Marinoni, C., McCracken, H., Memeo, P., Meneux, B., Nair, P., Porciani, C., Presotto, V., and Scaramella, R. (2010). Mass and Environment as Drivers of Galaxy Evolution in SDSS and zCOSMOS and the Origin of the Schechter Function. , 721(1):193–221.

Peng, Y.-j. and Renzini, A. (2020). Disc growth and quenching. , 491(1):L51–L55.

Pentericci, L., McLure, R. J., Garilli, B., Cucciati, O., Franzetti, P., Iovino, A., Amorin, R., Bolzonella, M., Bongiorno, A., Carnall, A. C., Castellano, M., Cimatti, A., Cirasuolo, M., Cullen, F., De Barros, S., Dunlop, J. S., Elbaz, D., Finkelstein, S. L., Fontana, A., Fontanot, F., Fumana, M., Gargiulo, A., Guaita, L., Hartley, W. G.,

Jarvis, M. J., Juneau, S., Karman, W., Maccagni, D., Marchi, F., Marmol-Queralto, E., Nandra, K., Pompei, E., Pozzetti, L., Scodeggio, M., Sommariva, V., Talia, M., Almaini, O., Balestra, I., Bardelli, S., Bell, E. F., Bourne, N., Bowler, R. A. A., Brusa, M., Buitrago, F., Caputi, K. I., Cassata, P., Charlot, S., Citro, A., Cresci, G., Cristiani, S., Curtis-Lake, E., Dickinson, M., Fazio, G. G., Ferguson, H. C., Fiore, F., Franco, M., Fynbo, J. P. U., Galametz, A., Georgakakis, A., Giavalisco, M., Grazian, A., Hathi, N. P., Jung, I., Kim, S., Koekemoer, A. M., Khusanova, Y., Le Fèvre, O., Lotz, J. M., Mannucci, F., Maltby, D. T., Matsuoka, K., McLeod, D. J., Mendez-Hernandez, H., Mendez-Abreu, J., Mignoli, M., Moresco, M., Mortlock, A., Nonino, M., Pannella, M., Papovich, C., Popesso, P., Rosario, D. P., Salvato, M., Santini, P., Schaerer, D., Schreiber, C., Stark, D. P., Tasca, L. A. M., Thomas, R., Treu, T., Vanzella, E., Wild, V., Williams, C. C., Zamorani, G., and Zucca, E. (2018). The VANDELS ESO public spectroscopic survey: Observations and first data release. , 616:A174.

Salim, S., Tacchella, S., Osborne, C., Faber, S. M., Lee, J. C., and Ellison, S. L. (2023). Σ_{SFR}-M $_*$ Diagram: A Valuable Galaxy Evolution Diagnostic to Complement (s)SFR-M $_*$ Diagrams. , 958(2):183.

Santini, P., Fontana, A., Castellano, M., Di Criscienzo, M., Merlin, E., Amorin, R., Cullen, F., Daddi, E., Dickinson, M., Dunlop, J. S., Grazian, A., Lamastra, A., McLure, R. J., Michałowski, M. J., Pentericci, L., and Shu, X. (2017). The Star Formation Main Sequence in the Hubble Space Telescope Frontier Fields. , 847(1):76.

Schawinski, K., Thomas, D., Sarzi, M., Maraston, C., Kaviraj, S., Joo, S.-J., Yi, S. K., and Silk, J. (2007). Observational evidence for AGN feedback in early-type galaxies. , 382(4):1415–1431.

Schreiber, C., Glazebrook, K., Nanayakkara, T., Kacprzak, G. G., Labbé, I., Oesch, P., Yuan, T., Tran, K. V., Papovich, C., Spitler, L., and Straatman, C. (2018). Near infrared spectroscopy and star-formation histories of 3 ≤ z ≤ 4 quiescent galaxies. , 618:A85.

Shah, E. A., Lemaux, B., Forrest, B., Cucciati, O., Hung, D., Staab, P., Hathi, N., Lubin, L., Gal, R. R., Shen, L., Zamorani, G., Giddings, F., Bardelli, S., Pasqua Cassara, L., Cassata, P., Contini, T., Golden-Marx, E., Guaita, L., Gururajan, G., Koekemoer, A. M., McLeod, D., Tasca, L. A. M., Tresse, L., Vergani, D., and Zucca, E. (2023). Identification and Characterization of Six Spectroscopically Confirmed Massive Protostructures at 2.5 < z < 4.5. *arXiv e-prints*, page arXiv:2312.04634.

Shahidi, A., Mobasher, B., Nayyeri, H., Hemmati, S., Wiklind, T., Chartab, N., Dickinson, M., Finkelstein, S. L., Pacifici, C., Papovich, C., Ferguson, H. C., Fontana, A., Giavalisco, M., Koekemoer, A., Newman, J., Sattari, Z., and Somerville, R. (2020). Selection of Massive Evolved Galaxies at 3 ≤ z ≤ 4.5 in the CANDELS Fields. , 897(1):44.

Straatman, C. M. S., Labbé, I., Spitler, L. R., Allen, R., Altieri, B., Brammer, G. B., Dickinson, M., van Dokkum, P., Inami, H., Glazebrook, K., Kacprzak, G. G., Kawinwanichakij, L., Kelson, D. D., McCarthy, P. J., Mehrtens, N., Monson, A.,

Murphy, D., Papovich, C., Persson, S. E., Quadri, R., Rees, G., Tomczak, A., Tran, K.-V. H., and Tilvi, V. (2014). A Substantial Population of Massive Quiescent Galaxies at z ∼4 from ZFOURGE. , 783(1):L14.

Talia, M., Schreiber, C., Garilli, B., Pentericci, L., Pozzetti, L., Zamorani, G., Cullen, F., Moresco, M., Calabrò, A., Castellano, M., Fynbo, J. P. U., Guaita, L., Marchi, F., Mascia, S., McLure, R., Mignoli, M., Pompei, E., Vanzella, E., Bongiorno, A., Vietri, G., Amorín, R. O., Bolzonella, M., Carnall, A. C., Cimatti, A., Cresci, G., Cristiani, S., Cucciati, O., Dunlop, J. S., Fontanot, F., Franzetti, P., Gargiulo, A., Hamadouche, M. L., Hathi, N. P., Hibon, P., Iovino, A., Koekemoer, A. M., Mannucci, F., McLeod, D. J., and Saldana-Lopez, A. (2023). The VANDELS ESO public spectroscopic survey: The spectroscopic measurements catalogue. , 678:A25.

Valentino, F., Tanaka, M., Davidzon, I., Toft, S., Gómez-Guijarro, C., Stockmann, M., Onodera, M., Brammer, G., Ceverino, D., Faisst, A. L., Gallazzi, A., Hayward, C. C., Ilbert, O., Kubo, M., Magdis, G. E., Selsing, J., Shimakawa, R., Sparre, M., Steinhardt, C., Yabe, K., and Zabl, J. (2020). Quiescent Galaxies 1.5 Billion Years after the Big Bang and Their Progenitors. , 889(2):93.

van der Burg, R. F. J., Muzzin, A., Hoekstra, H., Wilson, G., Lidman, C., and Yee, H. K. C. (2014). A census of stellar mass in ten massive haloes at z ∼1 from the GCLASS Survey. , 561:A79.

van der Wel, A., Bell, E. F., Häussler, B., McGrath, E. J., Chang, Y.-Y., Guo, Y., McIntosh, D. H., Rix, H. W., Barden, M., Cheung, E., Faber, S. M., Ferguson, H. C., Galametz, A., Grogin, N. A., Hartley, W., Kartaltepe, J. S., Kocevski, D. D., Koekemoer, A. M., Lotz, J., Mozena, M., Peth, M. A., and Peng, C. Y. (2012). Structural Parameters of Galaxies in CANDELS. , 203(2):24.

van der Wel, A., Franx, M., van Dokkum, P. G., Skelton, R. E., Momcheva, I. G., Whitaker, K. E., Brammer, G. B., Bell, E. F., Rix, H. W., Wuyts, S., Ferguson, H. C., Holden, B. P., Barro, G., Koekemoer, A. M., Chang, Y.-Y., McGrath, E. J., Häussler, B., Dekel, A., Behroozi, P., Fumagalli, M., Leja, J., Lundgren, B. F., Maseda, M. V., Nelson, E. J., Wake, D. A., Patel, S. G., Labbé, I., Faber, S. M., Grogin, N. A., and Kocevski, D. D. (2014). 3D-HST+CANDELS: The Evolution of the Galaxy Size-Mass Distribution since z = 3. , 788(1):28.

Wechsler, R. H. and Tinker, J. L. (2018). The Connection Between Galaxies and Their Dark Matter Halos. , 56:435–487.

Weinmann, S. M., van den Bosch, F. C., Yang, X., and Mo, H. J. (2006). Properties of galaxy groups in the Sloan Digital Sky Survey - I. The dependence of colour, star formation and morphology on halo mass. , 366(1):2–28.

Wetzel, A. R., Tinker, J. L., and Conroy, C. (2012). Galaxy evolution in groups and clusters: star formation rates, red sequence fractions and the persistent bimodality. , 424(1):232–243.

Wetzel, A. R., Tinker, J. L., Conroy, C., and van den Bosch, F. C. (2013). Galaxy evolution in groups and clusters: satellite star formation histories and quenching time-scales in a hierarchical Universe. , 432(1):336–358.

Whitaker, K. E., Labbé, I., van Dokkum, P. G., Brammer, G., Kriek, M., Marchesini, D., Quadri, R. F., Franx, M., Muzzin, A., Williams, R. J., Bezanson, R., Illingworth, G. D., Lee, K.-S., Lundgren, B., Nelson, E. J., Rudnick, G., Tal, T., and Wake, D. A. (2011). The NEWFIRM Medium-band Survey: Photometric Catalogs, Redshifts, and the Bimodal Color Distribution of Galaxies out to z $\sim$3. , 735(2):86.

Williams, R. J., Quadri, R. F., Franx, M., van Dokkum, P., and Labbé, I. (2009). Detection of Quiescent Galaxies in a Bicolor Sequence from Z = 0-2. , 691(2):1879–1895.

Appendix A

Other Plots

A1 UVJ Diagram

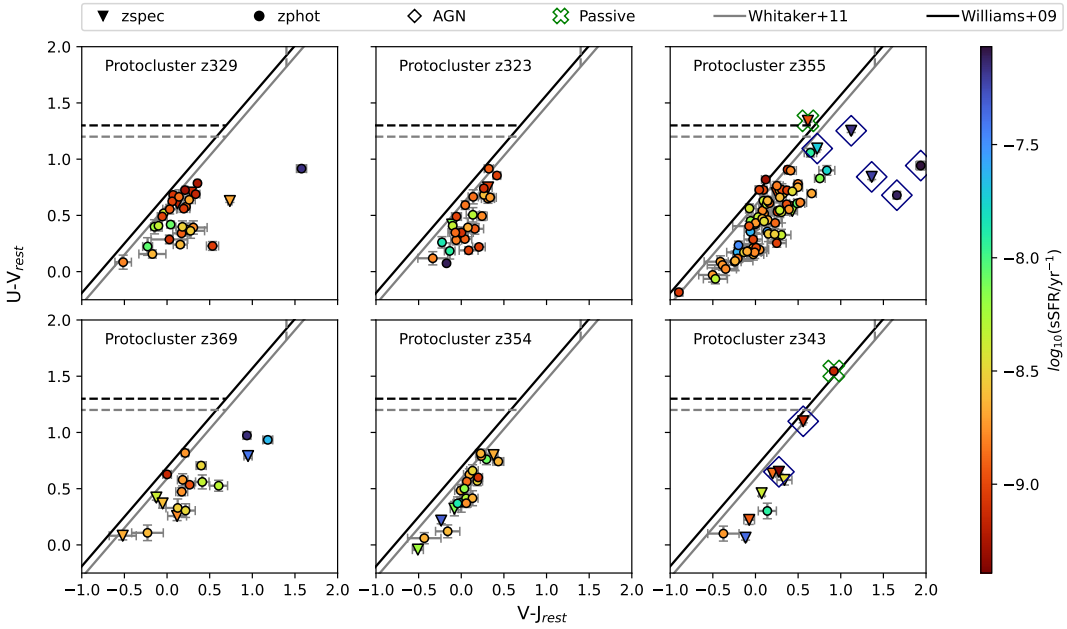

Figure A1.1: UVJ diagram showcasing member galaxies from protoclusters in the Chandra Deep Field South (CDFS). The color scale denotes log(sSFR), where red signifies lower values, and blue represents higher ones. Different shapes indicate the nature of the galaxies: triangles for spectroscopic redshift, dots for photometric redshift, diamonds for AGN, and crosses for passive galaxies. Lines on the diagram demarcate the criteria set by Williams et al. (2009) and Whitaker et al. (2011) for classification.

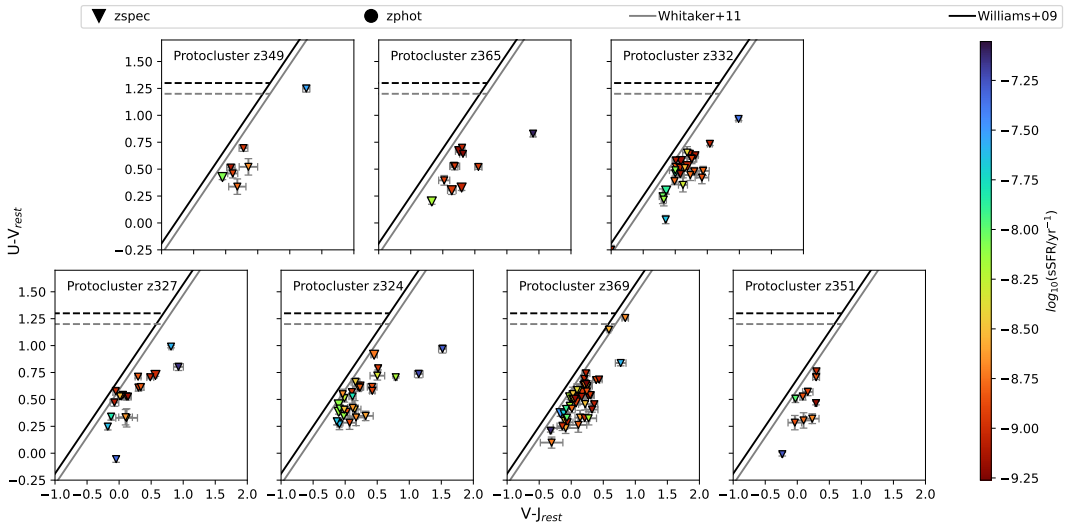

Figure A1.2: UVJ diagram showcasing member galaxies from protoclusters in the Ultra Deep Survey (UDS). The color scale denotes log(sSFR), where red signifies lower values, and blue represents higher ones. Different shapes indicate the nature of the galaxies: triangles for spectroscopic redshift, dots for photometric redshift. Lines on the diagram demarcate the criteria set by Williams et al. (2009) and Whitaker et al. (2011) for classification.

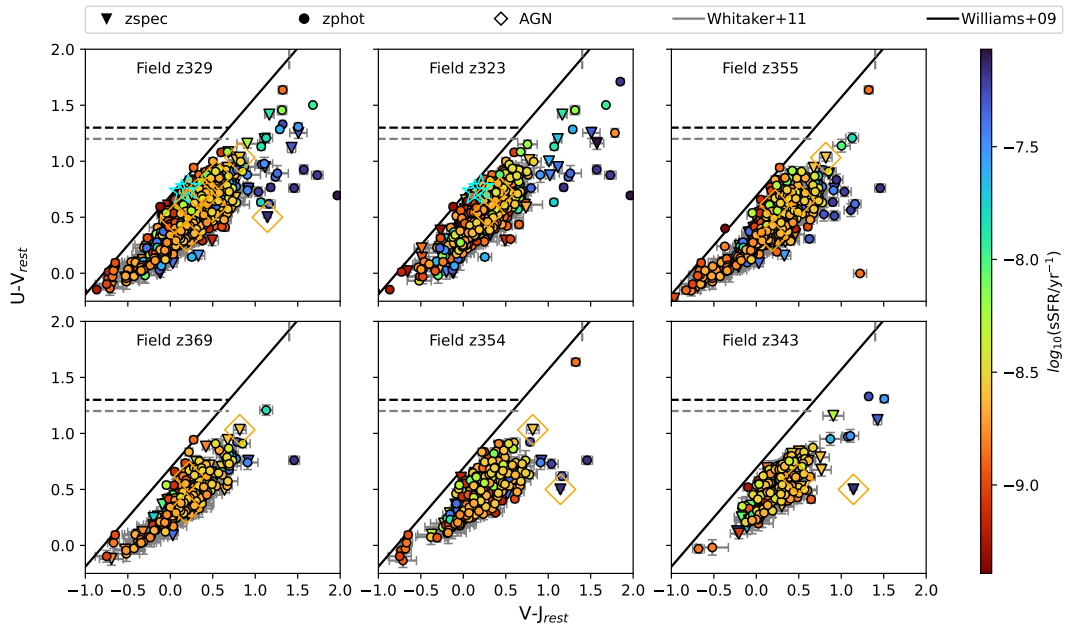

Figure A1.3: UVJ diagram of field galaxies from protoclusters in the Chandra Deep Field South (CDFS). The color scale represents log(sSFR), with red indicating lower values and blue indicating higher values. Different shapes indicate the nature of the galaxies: triangles for spectroscopic redshift, dots for photometric redshift, diamonds for AGN, and crosses for passive galaxies. Lines on the diagram demarcate the criteria set by Williams et al. (2009) and Whitaker et al. (2011) for classification.

A2 Redshift Distribution

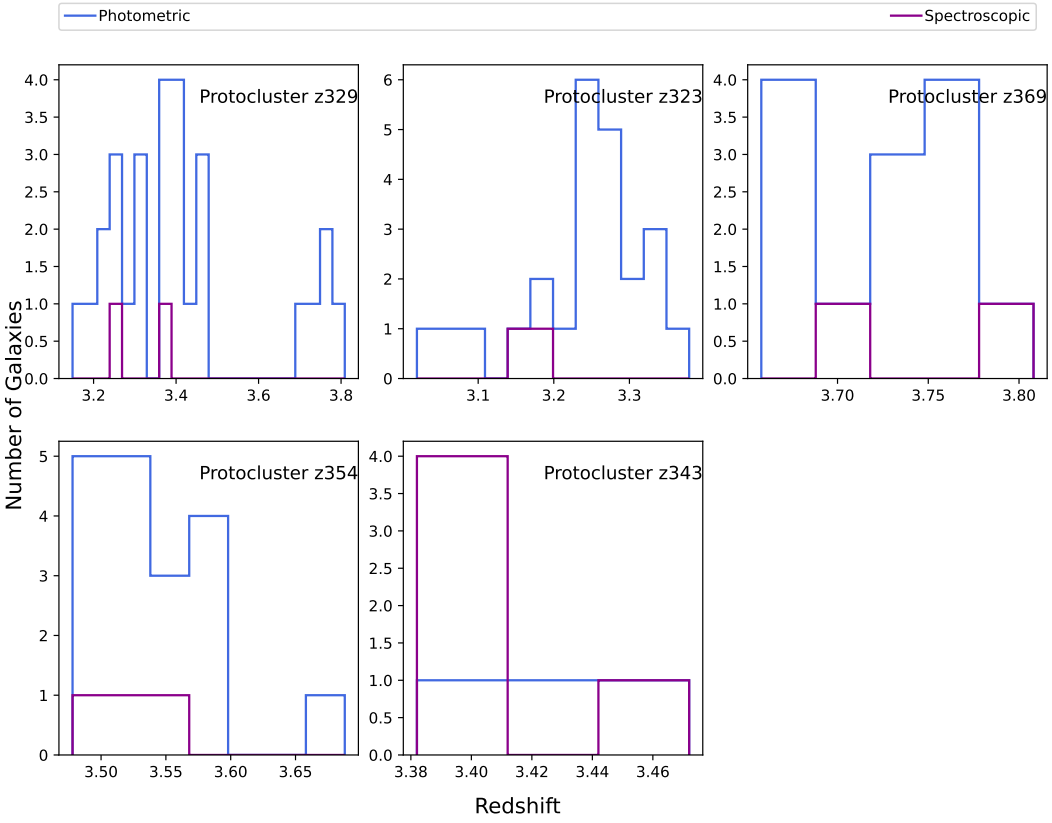

Figure A2.1: Histograms of redshift distributions for all identified overdensities in the CDFS region (except $z355$). Each histogram represents a different overdensity, showcasing the variations in redshift within these structures. For each overdensity, the distribution of photometric redshifts is illustrated in royal blue, while the distribution of spectroscopic redshifts is depicted in dark magenta.

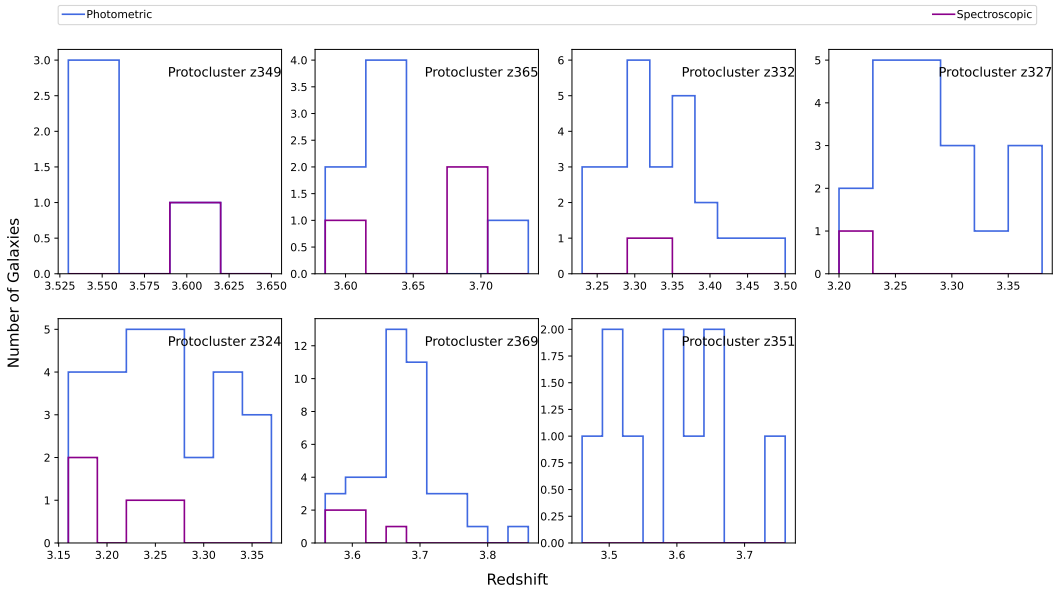

Figure A2.2: Histograms of redshift distributions for all identified overdensities in the UDS region. Each histogram represents a different overdensity, showcasing the variations in redshift within these structures. For each overdensity, the distribution of photometric redshifts is illustrated in royal blue, while the distribution of spectroscopic redshifts is depicted in dark magenta.